Progress In Electromagnetics Research, PIER 46, 203–244, 2004

NUMERICAL AND EXPERIMENTAL VALIDATIONS OF IEM FOR BISTATIC SCATTERING FROM NATURAL AND MANMADE ROUGH SURFACES

F. Koudogbo [†] **and P. F. Combes**

UPS-AD2M-IGEEP
118 Route de Narbonne, 31062 Toulouse Cedex 4, France

H.-J. Mametsa

ONERA-DEMR
2 Avenue Edouard Belin, 31055 Toulouse Cedex 4, France

Abstract—The Integral Equation Method (IEM) is applied for about ten years to model the surface scattering phenomenon. Recently, Fung published in [1] an extra improved version of the IEM model.

In this paper, numerical and experimental validations of the model are investigated. In backscattering, as in bistatic scattering, number of numerical validations are made on a wide frequency band, by comparing IEM predictions with a reference method results (Method of Moments). IEM results are also compared with those of some asymptotic models such as Small Perturbation Method (SPM) and Kirchhoff Model (KM) in the frequency domains where these latter are applicable.

The improved model validation is achieved by presenting confrontations of the simulation results with experimental data, some of them have been collected in appropriate papers, and the others come from experiments we conducted at the ElectroMagnetism and Radar Department (DEMR) of the *Office National d'Etudes et de Recherches Aérospatiales* (ONERA)-Toulouse (France).

[†] Also with ONERA-DEMR, 2 Avenue Edouard Belin, 31055 Toulouse Cedex 4, France

1 Introduction

2 Surface Scattering Coefficient Calculation for Small or Moderate Roughness ($ks_z \leq 2$)
- 2.1 Model Development
- 2.2 Coherent Scattering Coefficient Calculation
- 2.3 Incoherent Scattering Coefficient Calculation
  - 2.3.1 Evaluation of the Kirchhoff Term
  - 2.3.2 Evaluation of the Complementary Term
  - 2.3.3 Evaluation of the Cross Term
- 2.4 Surface Scattering Coefficient Summary
  - 2.4.1 The Single Scattering Coefficient
  - 2.4.2 The Multiple Scattering Coefficient

3 Numerical Simulations by IEM, SPM and KM of the Surface Scattering Coefficient Behavior, Compared with MM and Experimental Data
- 3.1 The Backscattering Case
  - 3.1.1 Comparisons with SPM and KM
  - 3.1.2 Parametrical Study of the Backscattering Coefficient
  - 3.1.3 Comparisons with Experimental Results and Validation
- 3.2 The Bistatic Case
  - 3.2.1 Comparisons with SPM and KM
  - 3.2.2 Comparisons with an Exact Method
  - 3.2.3 Parametrical Study of the Scattering Coefficient
  - 3.2.4 Comparisons with Experimental Results and Validation
- 3.3 Conclusion on the Numerical Study

4 Experimental Illustrations of the Surface Scattering Coefficient Behavior and IEM Validation
- 4.1 Presentation of the Measurements Setup
- 4.2 Characterization of the Samples
  - 4.2.1 Presentation
  - 4.2.2 Roughness and Dielectric Parameters Measurement
- 4.3 Results of the Experimental Study in Backscattering and Forward Scattering
  - 4.3.1 Case of ES Sample

4.3.2 Case of BBTM Sample
4.3.3 Conclusion on This Experimental Study and IEM Validation

5 Conclusion

Acknowledgment

Appendix A. The Field Coefficients Expressions
A.1 Expressions of Kirchhoff Coefficients
A.2 Expressions of Complementary Coefficients

References

1. INTRODUCTION

Early approaches to the theory of rough surface scattering were based on asymptotic approximations. In the low-frequency limit, Rice proposed the use of the Small Perturbation Method (SPM) [2]. At high frequencies, the Kirchhoff Model (KM) can be applied when the surface appears smooth on the scale of the wavelength [3, 4]. Much work over the past several decades has been devoted towards searching model which can assure the continuity between SPM and KM [5–7]. On the other hand, as scattering elements of rough surfaces present a complex geometry and are randomly distributed, their electromagnetic scattering involves complex interactions. Thus, this context leads us to focus our investigation in the rigorous model of the Integral Equation Method (IEM).

The first complete version of the IEM model was developed and proposed by A. K. Fung in [8] and [9], based on a more rigorous solution of the integral equation of the electric field. In this model, a simplifying assumption was made on the spectral form of the Green function [10], by ignoring the phase term, as it is shown in (1).

$$G(u,\, v) = -\frac{1}{2\pi} \int \frac{\mathrm{j}}{q}\, \mathrm{e}^{\mathrm{j}[u\,(x'-x'')+v\,(y'-y'')]}\, \underbrace{\mathrm{e}^{-\mathrm{j}q|z'-z''|}}_{\text{phase term}}\, dudv \qquad (1)$$

where

$$q = \sqrt{k^2 - u^2 - v^2} \qquad (2)$$

z' and z'' are the random variables representing the surface heights at different locations on the random surface, u and v are spatial variables and k is the wave number.

This approximation is valid and useful in backscattering and forward scattering calculations [8], but turns out to be false for bistatic and multiple scattering modeling. Thus, some additional studies were led by the principal authors of IEM in order to take into account in a better way the interactions between the surface and the incident wave [11–14], but some of these models still show some hiatuses in their theoretical formulations.

In 2001, Álvarez-Pérez [15] proposed an other model of IEM, including the phase term and some other modifications; following this previous article, Fung has recently published an improved IEM model [1].

The objectives of this study is to analyse this improved IEM model and compare the numerical results obtained with experimental data published in litterature or acquired by ourselves at the Electromagnetism and Radar Department (DEMR) of ONERA-Toulouse (France).

In the following section the most important theoretical results obtained by the development of IEM are briefly recalled. The third section is devoted to numerical simulations of the behavior of scattering by rough surfaces. A comparative study between IEM, KM and SPM is led on a wide range of frequencies, in monostatic and in bistatic cases, in order to demonstrate that IEM tends to bridge the gap between the two classical methods. Then, in bistatic case, the evolutions of the coherent and incoherent scattering mechanisms are observed and compared according to the surface roughness. Finally, in order to complete the validation of the IEM model, simulation results are confronted with some experimental values, some of them are taken from litterature, and the others come from measurements we realized at the DEMR. Discussions and concluding remarks are given in Section 5.

2. SURFACE SCATTERING COEFFICIENT CALCULATION FOR SMALL OR MODERATE ROUGHNESS ($ks_z \leq 2$)

2.1. Model Development

The Integral Equation Method or IEM is worked out to calculate the surface scattering of a given medium. This method gives a solution of the Stratton-Chu integral equation [16] through a reformulation of the governing equations of the tangential electric and magnetic surface fields (3), (4) [17]. They are expressed as a sum of two terms: the field calculated by the Kirchhoff Model and a complementary term which takes into account the wave interactions with the surrounding

roughness [9].

$$(\widehat{n} \wedge \overrightarrow{E}) = (\widehat{n} \wedge \overrightarrow{E})_k + (\widehat{n} \wedge \overrightarrow{E})_c \tag{3}$$

$$(\widehat{n} \wedge \overrightarrow{H}) = (\widehat{n} \wedge \overrightarrow{H})_k + (\widehat{n} \wedge \overrightarrow{H})_c \tag{4}$$

Accordingly, the scattered electric field, which is obtained by an estimation of the surface tangential fields, can be written as shown in (5). This formulation allows to obtain a more rigorous solution than those calculated by the more classical analytical methods; its validity domain overlaps those of Kirchhoff and Small Perturbation methods [18, 9].

$$E^s_{\mathrm{qp}} = E^{sk}_{\mathrm{qp}} + E^{sc}_{\mathrm{qp}} \tag{5}$$

E^{sk}_{qp} is the Kirchhoff field and E^{sc}_{qp} is the complementary field, they are expressed by,

$$E^{sk}_{\mathrm{qp}} = KE_0 \int_{S'} f_{\mathrm{qp}}\, \mathrm{e}^{\mathrm{j}[(\vec{k}_s - \vec{k}_i)\cdot\vec{r'}]}\, dx'\, dy' \tag{6}$$

$$E^{sc}_{\mathrm{qp}} = \frac{KE_0}{8\pi^2} \int\int_{S'} \int_{S''} F_{\mathrm{qp}}\, \mathrm{e}^{\mathrm{j}[u\,(x'-x'')+v\,(y'-y'')-q|z'-z''|]} \times \mathrm{e}^{\mathrm{j}[\vec{k}_s\cdot\vec{r'} - \vec{k}_i\cdot\vec{r''}]}\, dx''\, dy''\, dx'\, dy'\, du\, dv \tag{7}$$

where

$$K = -\frac{\mathrm{j}k}{4\pi R}\, \mathrm{e}^{-jkR}$$

R is the distance between emitting and receiving antennas.

The subscripts p and q respectively denote the polarizations of the emitting and receiving antennas.

In the above scattered field expressions, f_{qp} and F_{qp} are respectively called Kirchhoff and complementary coefficients [9]. Their expressions are reported in Appendix A at the end of this paper.

The average scattered power is calculated from the electric scattered field by the well-known following relation,

$$P^s_{\mathrm{qp}} = \frac{1}{2\eta_1} \langle E^s_{\mathrm{qp}}\, E^{s*}_{\mathrm{qp}} \rangle \tag{8}$$

where η_1 is the intrinsic impedance of the medium and "$*$" is the symbol for complex conjugate.

With the field expression given by (5), the average scattered power (8) is expressed as the sum of three terms:

$$P^s_{\mathrm{qp}} = \frac{1}{2\eta_1} \left[\langle E^{sk}_{\mathrm{qp}}\, E^{sk*}_{\mathrm{qp}} \rangle + 2\mathcal{R}e \langle E^{sc}_{\mathrm{qp}}\, E^{sk*}_{\mathrm{qp}} \rangle + \langle E^{sc}_{\mathrm{qp}}\, E^{sc*}_{\mathrm{qp}} \rangle \right] = P^{sk}_{\mathrm{qp}} + P^{skc}_{\mathrm{qp}} + P^{sc}_{\mathrm{qp}} \tag{9}$$

where $\mathcal{R}e$ is the real part operator. The powers related to E^{sk}_{qp} and E^{sc}_{qp} are respectively called Kirchhoff power and complementary power. The power related to the both fields is called cross power.

On the other hand, the scattering process is composed of two types of mechanisms [4]: the coherent scattering and the incoherent scattering (Fig. 1),

$$P^{s}_{\mathrm{qp}} = P^{s}_{\mathrm{qp}_{coh}} + P^{s}_{\mathrm{qp}_{incoh}} \tag{10}$$

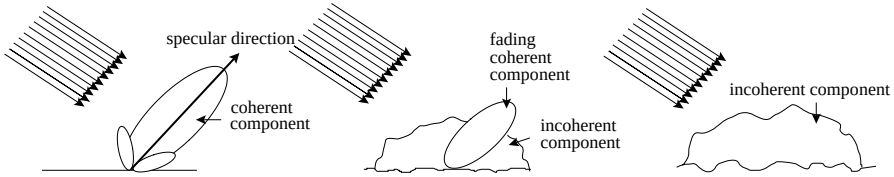

Figure 1. Evolution of the scattering according to the surface roughness.

The coherent scattered power $P^{s}_{\mathrm{qp}_{coh}}$ is the power scattered in the specular lobe. It decreases when the roughness increases and is calculated from the mean squared power as follows,

$$\begin{aligned} P^{s}_{\mathrm{qp}_{coh}} &= \frac{1}{2\eta_1} \langle E^{s}_{\mathrm{qp}} \rangle \langle E^{s*}_{\mathrm{qp}} \rangle \\ &= \frac{1}{2\eta_1} \left[\langle E^{sk}_{\mathrm{qp}} \rangle \langle E^{sk*}_{\mathrm{qp}} \rangle + 2\mathcal{R}e \langle E^{sc}_{\mathrm{qp}} \rangle \langle E^{sk*}_{\mathrm{qp}} \rangle + \langle E^{sc}_{\mathrm{qp}} \rangle \langle E^{sc*}_{\mathrm{qp}} \rangle \right] \\ &= P^{sk}_{\mathrm{qp}_{coh}} + P^{skc}_{\mathrm{qp}_{coh}} + P^{sc}_{\mathrm{qp}_{coh}} \end{aligned} \tag{11}$$

The incoherent contribution, which represents the power scattered outwards the specular, is obtained by subtracting the previous coherent power from the total power (12). It increases with the roughness.

$$\begin{aligned} P^{s}_{\mathrm{qp}_{incoh}} &= \frac{1}{2\eta_1} \left[\langle E^{s}_{\mathrm{qp}} E^{s*}_{\mathrm{qp}} \rangle - \langle E^{s}_{\mathrm{qp}} \rangle \langle E^{s*}_{\mathrm{qp}} \rangle \right] \\ &= P^{sk}_{\mathrm{qp}_{incoh}} + P^{skc}_{\mathrm{qp}_{incoh}} + P^{sc}_{\mathrm{qp}_{incoh}} \end{aligned} \tag{12}$$

Finally, the calculation of the total scattered power can be schematically summarized by Fig. 2.

The normalized scattering coefficient is related to the scattered average power by,

$$\sigma^{0}_{\mathrm{qp}} = \frac{4\pi R^2 P^{s}_{\mathrm{qp}}}{A_0 P^{i}_{\mathrm{p}}} \tag{13}$$

where $P^{i}_{\mathrm{p}} = \frac{1}{2\eta_1} E_0^2$ is the incident power and A_0 is the illuminated area.

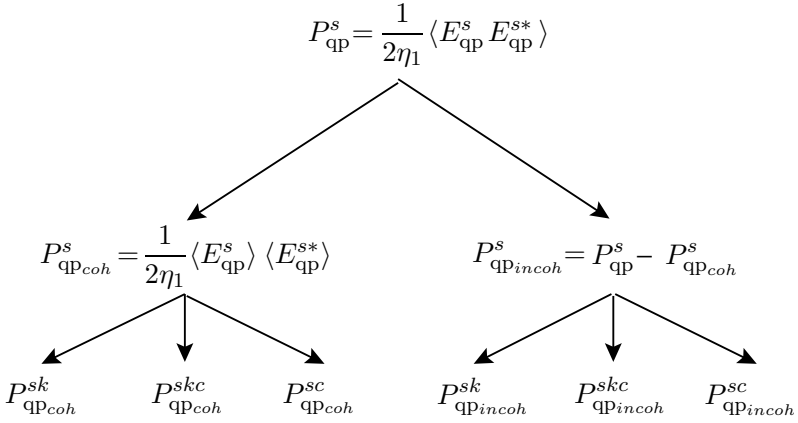

Figure 2. Total scattered power calculation by IEM.

Two forms of IEM have been developped by Fung and his colleagues, one for small to moderate scale roughness ($ks_z \leq 2$), and the other for large scale roughness. In the following sections, the coherent and incoherent scattering mechanisms are separately considered from smooth to moderately rough surfaces. The expressions of the Kirchhoff, complementary and cross terms of each contribution are recalled.

2.2. Coherent Scattering Coefficient Calculation

The coherent scattered power is calculated from (11). The three terms in that equation must be evaluated one by one. However Figs. 3 and 4 clearly show that the complementary and the cross terms are insignificant in comparison with the Kirchhoff term whatever the surface roughness. This may be explained by the fact that complementary field allows to take into account multiple scattering, which does not occur in a coherent way.

The coherent power is then simply expressed by,

$$P^s_{\mathrm{qp}_{coh}} = P^{sk}_{\mathrm{qp}_{coh}} = \frac{1}{2\eta_1}\left[\langle E^{sk}_{\mathrm{qp}}\rangle \langle E^{sk*}_{\mathrm{qp}}\rangle\right] \tag{14}$$

To carry out the average operations, the height distributions of the concerned surfaces are assumed to be Gaussian. Wave numbers of incidence and scattering are defined as $\vec{k}_i = k_x\hat{x} + k_y\hat{y} - k_z\hat{z}$ and $\vec{k}_s = k_{sx}\hat{x} + k_{sy}\hat{y} + k_{sz}\hat{z}$.

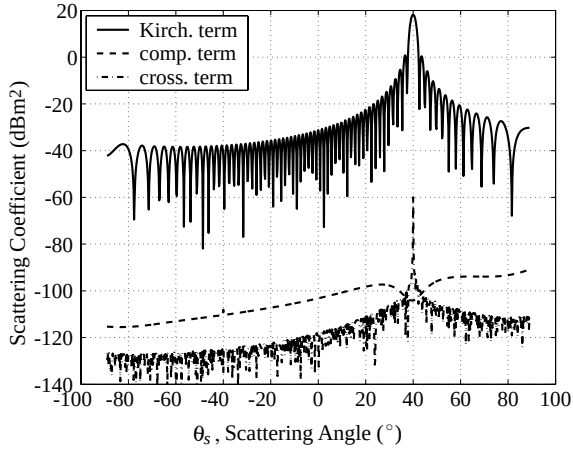

Figure 3. Evolution of the coherent scattering terms for a slightly rough conducting surface.

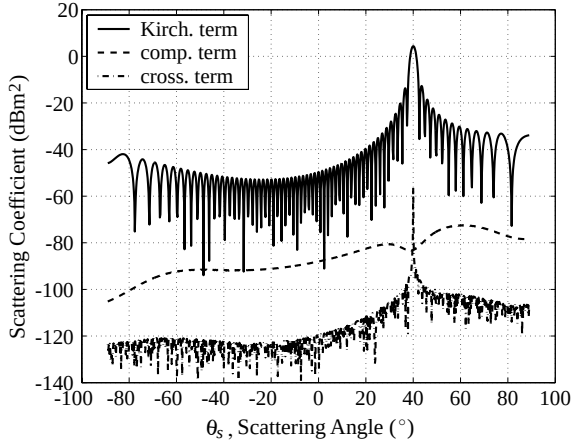

Figure 4. Evolution of the coherent scattering terms for a rough conducting surface.

Thus replacing in (14) the Kirchhoff field by its expression leads to,

$$P_{\mathrm{qp}_{coh}}^{sk} = \frac{1}{2\eta_1} \left| KE_0 f_{\mathrm{qp}} \right|^2 \left| \left\langle \int_{S'} \mathrm{e}^{\mathrm{j}[(k_{sx}-k_x)x' + (k_{sy}-k_y)y' + (k_{sz}+k_z)z']} \, dx'dy' \right\rangle \right|^2 \tag{15}$$

The details of the calculations can be found in literature [19, 20], only the final results are given in the case of two different classical surface

geometries.

• In the case of a circular surface, $P^{sk}_{\mathrm{qp}_{coh}}$ is given by

$$P^{sk}_{\mathrm{qp}_{coh}} = \frac{1}{2\eta_1} \left|KE_0 f_{\mathrm{qp}}\right|^2 4A_0^2 \, \mathrm{e}^{-s_z^2(k_{sz}+k_z)^2} \left|\frac{\mathrm{J}_1(R_{max}\times \mathrm{M})}{R_{max}\times \mathrm{M}}\right|^2 \tag{16}$$

where $\mathrm{M} = \sqrt{(k_{sx}-k_x)^2+(k_{sy}-k_y)^2}$, $A_0 = \pi R^2_{max}$ is the illuminated area and J_m is the Bessel function of first kind and of m-order.

Applying (13) to this case leads to the scattering coefficient given by:

$$\sigma^{k0}_{\mathrm{qp}_{coh}} = \frac{k^2}{\pi} \left|f_{\mathrm{qp}}\right|^2 A_0^2 \, \mathrm{e}^{-s_z^2(k_{sz}+k_z)^2} \left|\frac{\mathrm{J}_1(R_{max}\times \mathrm{M})}{R_{max}\times \mathrm{M}}\right|^2 \tag{17}$$

• In the case of a rectangular surface, $P^{sk}_{\mathrm{qp}_{coh}}$ changes to:

$$\begin{aligned} P^{sk}_{\mathrm{qp}_{coh}} &= \frac{1}{2\eta_1} \left|KE_0 f_{\mathrm{qp}}\right|^2 A_0^2 \, \mathrm{e}^{-s_z^2(k_{sz}+k_z)^2} \\ &\quad \times \left|\sin_c\left[(k_{sx}-k_x)x_0\right] \, \sin_c\left[(k_{sy}-k_y)y_0\right]\right|^2 \end{aligned} \tag{18}$$

where $\sin_c \mathrm{u} = \frac{\sin \mathrm{u}}{\mathrm{u}}$ and $A_0 = 2x_0 \times 2y_0$.

The expression of the scattering coefficient from a rectangular surface is then,

$$\sigma^{k0}_{\mathrm{qp}_{coh}} = \frac{k^2}{\pi} \left|f_{\mathrm{qp}}\right|^2 A_0^2 \, \mathrm{e}^{-s_z^2(k_{sz}+k_z)^2} \left|\sin_c\left[(k_{sx}-k_x)x_0\right] \, \sin_c\left[(k_{sy}-k_y)y_0\right]\right|^2 \tag{19}$$

In the next subsection, the calculation of the three terms composing the incoherent scattering coefficient is briefly set out.

2.3. Incoherent Scattering Coefficient Calculation

The incoherent power is obtained by the following equation,

$$\begin{aligned} P^{s}_{\mathrm{qp}_{incoh}} &= P^{s}_{\mathrm{qp}} - P^{s}_{\mathrm{qp}_{coh}} \\ &= \frac{1}{2\eta_1} \left[\langle E^{s}_{\mathrm{qp}} \, E^{s*}_{\mathrm{qp}}\rangle - \langle E^{s}_{\mathrm{qp}}\rangle \, \langle E^{s*}_{\mathrm{qp}}\rangle\right] \end{aligned} \tag{20}$$

The calculation of the three terms are available in [9, 21, 15, 20], only the major steps and the final results are reported in this paper.

2.3.1. Evaluation of the Kirchhoff Term

First considering the Kirchhoff term given below by,

$$P^{sk}_{\mathrm{qp}_{incoh}} = \frac{1}{2\eta_1}\left[\langle E^{sk}_{\mathrm{qp}}\, E^{sk*}_{\mathrm{qp}}\rangle - \langle E^{sk}_{\mathrm{qp}}\rangle\, \langle E^{sk*}_{\mathrm{qp}}\rangle\right] \tag{21}$$

In the case of small or moderate roughness ($ks_z \leq 2$), it is a standard practice to expand the exponential terms in series [9], and then integrate over the spatial variables.

Finally the Kirchhoff term of the incoherent scattered power expression is,

$$\begin{aligned} P^{sk}_{\mathrm{qp}_{incoh}} &= 2\pi\, \frac{|KE_0 f_{\mathrm{qp}}|^2}{2\eta_1}\, \mathrm{e}^{-s_z^2(k_{sz}+k_z)^2} \\ &\quad \times A_0 \sum_{n=1}^{\infty} \frac{[s_z^2(k_{sz}+k_z)^2]^n}{n!}\, W^{(n)}(k_{sx}-k_x,\, k_{sy}-k_y) \end{aligned} \tag{22}$$

where $W^{(n)}(k_{sx}-k_x,\, k_{sy}-k_y)$ is the roughness spectrum of the surface related to the n^{th} power of the surface correlation function $\rho(\xi,\, \zeta)$ by the Fourier transform as follows,

$$W^{(n)}(k_{sx}-k_x,\, k_{sy}-k_y) = \frac{1}{2\pi} \int \rho^n(\xi,\, \zeta)\, \mathrm{e}^{\mathrm{j}[(k_{sx}-k_x)\xi + (k_{sy}-k_y)\zeta]}\, d\xi d\zeta \tag{23}$$

The Kirchhoff incoherent scattering coefficient is then deduced from (13) and (22),

$$\sigma^{k0}_{\mathrm{qp}_{incoh}} = \frac{k^2}{2}|f_{\mathrm{qp}}|^2 \mathrm{e}^{-s_z^2(k_{sz}+k_z)^2} \sum_{n=1}^{\infty} \frac{[s_z^2(k_{sz}+k_z)^2]^n}{n!} W^{(n)}(k_{sx}-k_x, k_{sy}-k_y) \tag{24}$$

2.3.2. Evaluation of the Complementary Term

The complementary power $P^{sc}_{\mathrm{qp}_{incoh}}$ is then considered,

$$P^{sc}_{\mathrm{qp}_{incoh}} = \frac{1}{2\eta_1}\left[\langle E^{sc}_{\mathrm{qp}}\, E^{sc*}_{\mathrm{qp}}\rangle - \langle E^{sc}_{\mathrm{qp}}\rangle\, \langle E^{sc*}_{\mathrm{qp}}\rangle\right] \tag{25}$$

The substitution of the complementary field by its expression (7) in (25) produces,

$$\begin{aligned} P^{sc}_{\mathrm{qp}_{incoh}} &= \frac{(2\pi)^5}{8\eta_1} \left|\frac{KE_0}{8\pi^2}\right|^2 A_0\, \mathrm{e}^{-s_z^2(k_{sz}+k_z)^2} \\ &\quad \times [c_1(q,q') + c_2(q,q') + c_3(q,q') + c_4(q,q') + c_5(q,q') + c_6(q,q')] \end{aligned} \tag{26}$$

Recalling that the q and q' coefficients are given by (2), the $c_{\rm i}(q,q')|_{i=1,\ldots,6}$ terms are expressed by,

$$\begin{aligned}
c_1(q,q') &= \sum_{r,\,r'=-1,\,1} h(rk_z,r'k_z)\; f_1(rk_z,r'k_z) \\
&\quad \times F_{\rm qp}(-k_x,-k_y,r)\; F^*_{\rm qp}(-k_x,-k_y,r') \qquad (27)\\
c_2(q,q') &= \sum_{r,\,r'=-1,\,1} h(rk_z,r'k_{sz})\; f_2(rk_z,r'k_{sz}) \\
&\quad \times F_{\rm qp}(-k_x,-k_y,r)\; F^*_{\rm qp}(-k_{sx},-k_{sy},r') \qquad (28)\\
c_3(q,q') &= \sum_{r,\,r'=-1,\,1} h(rk_{sz},r'k_z)\; f_3(rk_{sz},r'k_z) \\
&\quad \times F_{\rm qp}(-k_{sx},-k_{sy},r)\; F^*_{\rm qp}(-k_x,-k_y,r') \qquad (29)\\
c_4(q,q') &= \sum_{r,\,r'=-1,\,1} h(rk_{sz},r'k_{sz})\; f_4(rk_{sz},r'k_{sz}) \\
&\quad \times F_{\rm qp}(-k_{sx},-k_{sy},r)\; F^*_{\rm qp}(-k_{sx},-k_{sy},r') \qquad (30)\\
c_5(q,q') &= \frac{1}{2\pi} \sum_{r,\,r'=-1,\,1} \int [h(rq,r'q)\; f_1(rq,r'q)\; f_4(rq,r'q) \\
&\quad \times F_{\rm qp}(u,v,r)\; F^*_{\rm qp}(u,v,r')]\; dudv \qquad (31)\\
c_6(q,q') &= \frac{1}{2\pi} \sum_{r,\,r'=-1,\,1} \int [h(rq,r'q')\; f_2(rq,r'q')\; f_3(rq,r'q') \\
&\quad \times F_{\rm qp}(u,v,r)\; F^*_{\rm qp}(u',v',r')]\; dudv \qquad (32)
\end{aligned}$$

knowing that $u' = -u - k_{sx} - k_x$ and $v' = -v - k_{sy} - k_y$.

The different functions used in (27) to (32) are defined below

$$h(rq,r'q') = {\rm e}^{-s_z^2[q^2+q'^2-(k_{sz}-k_z)(rq+r'q')]} \qquad (33)$$

$$f_1(rq,r'q') = \sum_{n=1}^{\infty} \frac{[s_z^2(k_{sz}-rq)(k_{sz}-r'q')]^n}{n!} W^{(n)}(k_{sx}-k_x,k_{sy}-k_y) \qquad (34)$$

$$f_2(rq,r'q') = \sum_{n=1}^{\infty} \frac{[s_z^2(k_{sz}-rq)(k_z+r'q')]^n}{n!} W^{(n)}(k_{sx}-k_x,k_{sy}-k_y) \qquad (35)$$

$$f_3(rq,r'q') = \sum_{m=1}^{\infty} \frac{[s_z^2(k_z+rq)(k_{sz}-r'q')]^m}{m!} W^{(m)}(k_{sx}-k_x,k_{sy}-k_y) \qquad (36)$$

$$f_4(rq,r'q') = \sum_{m=1}^{\infty} \frac{[s_z^2(k_z+rq)(k_z+r'q')]^m}{m!} W^{(m)}(k_{sx}-k_x,k_{sy}-k_y) \qquad (37)$$

The scattering coefficient is calculated from (13), yielding:

$$\sigma^{c0}_{\mathrm{qp}_{incoh}} = \frac{k^2}{2^{10}\pi^5}\, A_0\, \mathrm{e}^{-s_z^2(k_{sz}+k_z)^2} \times [c_1(q,q') + c_2(q,q') + c_3(q,q') + c_4(q,q') + c_5(q,q') + c_6(q,q')] \tag{38}$$

$c_{\mathrm{i}}(q,q')|_{i=1,\ldots,6}$ are given by (27) through (32).

2.3.3. Evaluation of the Cross Term

The cross term is calculated from the expressions of both Kirchhoff and complementary fields by

$$P^{skc}_{\mathrm{qp}_{incoh}} = \frac{1}{2\eta_1}\, \Big[\langle E^{sc}_{\mathrm{qp}}\, E^{sk*}_{\mathrm{qp}}\rangle - \langle E^{sc}_{\mathrm{qp}}\rangle\, \langle E^{sk*}_{\mathrm{qp}}\rangle\Big] \tag{39}$$

The substitution of the two fields by their expressions (6) and (7) produces,

$$P^{skc}_{\mathrm{qp}_{incoh}} = \frac{(2\pi)^3}{2\eta_1}\, \frac{|KE_0|^2}{2^4\pi^2}\, A_0\, \mathrm{e}^{-s_z^2(k_{sz}^2+k_z^2+k_{sz}k_z)} \times \mathcal{R}e\Big\{kc_1(q) + kc_2(q) + kc_3(q)\Big\} \tag{40}$$

where

$$kc_1(q) = \sum_{r=-1,\,1} f_1'(rk_z)\, f^*_{\mathrm{qp}}\, F_{\mathrm{qp}}(-k_x,-k_y,r) \tag{41}$$

$$kc_2(q) = \sum_{r=-1,\,1} f_2'(rk_{sz})\, f^*_{\mathrm{qp}}\, F_{\mathrm{qp}}(-k_{sx},-k_{sy},r) \tag{42}$$

$$kc_3(q) = \frac{1}{2\pi} \sum_{r=-1,\,1} \int h'(rq) f_1'(rq)\, f_2'(rq)\, f^*_{\mathrm{qp}}\, F_{\mathrm{qp}}(u,v,rq)\, dudv \tag{43}$$

and

$$h'(rq) = \mathrm{e}^{-s_z^2[q^2-(k_{sz}-k_z)rq]} \tag{44}$$

$$f_1'(rq) = \sum_{n=1}^{\infty} \frac{\big[s_z^2(k_{sz}-rq)(k_{sz}+k_z)\big]^n}{n!}\, W^{(n)}(k_{sx}-k_x,\, k_{sy}-k_y) \tag{45}$$

$$f_2'(rq) = \sum_{n=1}^{\infty} \frac{\big[s_z^2(k_z+rq)(k_{sz}+k_z)\big]^n}{n!}\, W^{(n)}(k_{sx}-k_x,\, k_{sy}-k_y) \tag{46}$$

Using (13), the scattering cross coefficient is then:

$$\sigma^{kc0}_{\mathrm{qp}_{incoh}} = \frac{k^2}{2^5\pi^3}\, \mathrm{e}^{-s_z^2(k_{sz}^2+k_z^2+k_{sz}k_z)}\, \mathcal{R}e\Big\{kc_1(q) + kc_2(q) + kc_3(q)\Big\} \tag{47}$$

$kc_{\mathrm{i}}(q)|_{i=1,\ldots,3}$ are given by (41) through (43).

2.4. Surface Scattering Coefficient Summary

The complete representation of the bistatic scattering coefficient for a randomly rough surface can be summarized as:

$$\begin{aligned}\sigma^0_{\mathrm{qp}} &= \sigma^0_{\mathrm{qp}_{incoh}} + \sigma^0_{\mathrm{qp}_{coh}} \\ &= (\sigma^{k0}_{\mathrm{qp}_{incoh}} + \sigma^{k0}_{\mathrm{qp}_{coh}}) + \sigma^{kc0}_{\mathrm{qp}_{incoh}} + \sigma^{c0}_{\mathrm{qp}_{incoh}} \\ &= \sigma^{0(S)}_{\mathrm{qp}} + \sigma^{0(M)}_{\mathrm{qp}}\end{aligned} \tag{48}$$

The terms are regrouped into two types: one representing single scattering $\sigma^{0(S)}_{\mathrm{qp}}$, and the other representing multiple scattering $\sigma^{0(M)}_{\mathrm{qp}}$ (Fig. 5). The former corresponds to terms already integrated whereas the latter involves more than one sum and requires further integrations. Second-order scattering is considered at most.

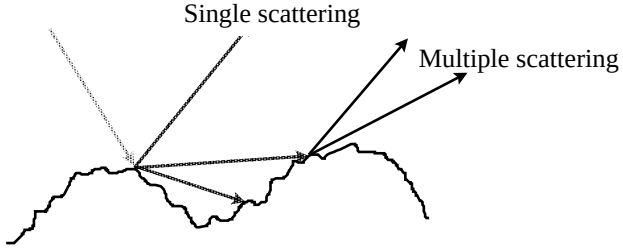

Figure 5. Surface scattering mechanisms.

2.4.1. The Single Scattering Coefficient

The single scattering coefficient $\sigma^{0(S)}_{\mathrm{qp}}$ is the sum of the coherent scattering coefficient and the first-order incoherent scattering coefficient. The first one is given by (17) or (19) according to the geometry of the surface.

The first-order incoherent coefficient is the sum of the Kirchhoff term and the terms already integrated of $\sigma^{c0}_{\mathrm{qp}_{incoh}}$ and $\sigma^{kc0}_{\mathrm{qp}_{incoh}}$. Its

expression is,

$$\sigma^{0(S)}_{\mathrm{qp}_{incoh}} = \frac{k^2}{2}|f_{\mathrm{qp}}|^2 \mathrm{e}^{-s_z^2(k_{sz}+k_z)^2} \sum_{n=1}^{\infty} \frac{[s_z^2(k_{sz}+k_z)^2]^n}{n!} W^{(n)}(k_{sx}-k_x, k_{sy}-k_y)$$
$$+\frac{k^2}{2^{10}\pi^5}\, \mathrm{e}^{-s_z^2(k_{sz}^2+k_z^2)}[c_1(q,q') + c_2(q,q') + c_3(q,q') + c_4(q,q')]$$
$$+\frac{k^2}{2^5\pi^3}\, \mathrm{e}^{-s_z^2(k_{sz}^2+k_z^2+k_{sz}k_z)} \mathcal{R}e\Big\{kc_1(q) + kc_2(q)\Big\} \tag{49}$$

$c_i(q,q')|_{i=1,\ldots,4}$ and $kc_j(q)|_{j=1,2}$ are respectively given by (27) to (30) and by (41) and (42).

Combining the different terms in an appropriate way [9] leads to the following expression,

$$\sigma^{0(S)}_{\mathrm{qp}_{incoh}} = \frac{k^2}{2}\, \mathrm{e}^{-s_z^2(k_{sz}^2+k_z^2)} \sum_{n=1}^{\infty} s_z^{2n}\, |I^{(n)}_{\mathrm{qp}}|^2 \frac{W^{(n)}(k_{sx}-k_x,\, k_{sy}-k_y)}{n!} \tag{50}$$

where

$$I^{(n)}_{\mathrm{qp}} = (k_{sz}+k_z)^n f_{\mathrm{qp}}\, \mathrm{e}^{-s_z^2 k_{sz} k_z}$$
$$+\frac{1}{4} \sum_{r=-1,\,1} [\mathrm{e}^{-s_z^2[q^2-(k_{sz}-k_z)rq]}(k_{sz}-rq)^n F_{\mathrm{qp}}(-k_x,-k_y,rq)$$
$$+\mathrm{e}^{-s_z^2[q^2-(k_{sz}-k_z)rq]}(k_z+rq)^n F_{\mathrm{qp}}(-k_{sx},-k_{sy},rq)] \tag{51}$$

The single scattering coefficient is the most important term in co-polarized backscattering and forward scattering coefficients. In this polarization the multiple scattering contribution is generally small. On the other hand, in cross polarization, the multiple scattering contribution is the most important one in backscattering and forward scattering coefficients, because the single scattering coefficient vanishes in the incident plane. The multiple scattering component is evaluated in the next subsection.

2.4.2. The Multiple Scattering Coefficient

Only the terms of the complementary and the cross terms requiring further integrations compose the coefficient representing multiple scattering [14, 21–23]. So from (38) and (47), the coefficient is given by the following three terms,

$$\sigma^{0(M)}_{\mathrm{qp}_{incoh}} = \frac{k^2}{2^{10}\pi^5}\, \mathrm{e}^{-s_z^2(k_{sz}^2+k_z^2)}\, [c_5(q,q') + c_6(q,q')]$$
$$+\frac{k^2}{2^5\pi^3}\, \mathrm{e}^{-s_z^2(k_{sz}^2+k_z^2+k_{sz}k_z)}\, \mathcal{R}e\{kc_3(q)\} \tag{52}$$

$c_5(q,q')$, $c_6(q,q')$ and $kc_3(q)$ are respectively given by (31), (32) and (43).

In this section, scattering coefficients expressions were deduced from theoretical formulations of the total scattered power, using an improved IEM model. The two following sections are devoted to the validation of the model. In Section 3, numerical simulations of the scattering coefficient behavior are made: either in monostatic case, or in the bistatic one, IEM results are confronted with those of other methods in order to demonstrate the extent of the applicability domain of the model. In Section 4 experimental validation of the IEM model is investigated.

3. NUMERICAL SIMULATIONS BY IEM, SPM AND KM OF THE SURFACE SCATTERING COEFFICIENT BEHAVIOR, COMPARED WITH MM AND EXPERIMENTAL DATA

3.1. The Backscattering Case

3.1.1. Comparisons with SPM and KM

Figs. 6, 7 and 8 show the evolution of backscattering coefficients from Gaussian correlated perfectly conducting surfaces. The numerical results obtained by IEM are compared with those obtained by SPM and KM on a wide frequency band. The limits of the validity domains of SPM and KM are illustrated by Table 1 [19].

Table 1. Applicability domains of SPM and KM for a Gaussian correlated surface.

Models	ks_z	kl_c
SPM	> 0.3	$> \frac{\sqrt{2}}{0.3} ks_z$
KM	$\frac{(kl_c)^2}{17.39}$	$> 2\pi$

The asymptotic models are also confronted with the Method of Moments (MM). These last results have been collected in [9].

First, it is worth noticing that, for all frequencies, the IEM predictions are in good agreement with the MM results.

Fig. 6 shows that when $ks_z < 0.3$ and $kl_c < \frac{\sqrt{2}}{0.3} ks_z$, SPM is in good agreement with IEM over most part of the angular range considered,

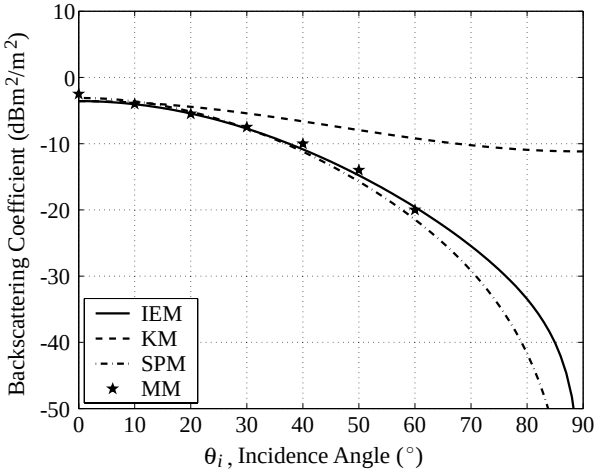

Figure 6. Comparisons of IEM, KM, SPM and MM in the frequency domain where SPM is applicable.

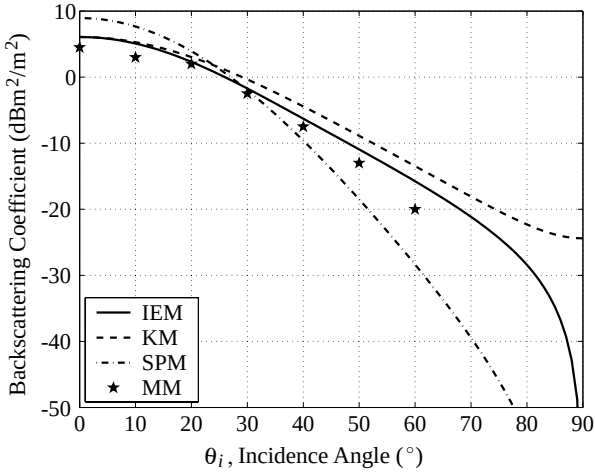

Figure 7. Comparisons of IEM, KM, SPM and MM in the frequency domain where neither SPM nor KM are applicable.

but deviates from the improved model at incident angles larger than 60°.

Then when the frequency increases by a factor of two (Fig. 7), the surface parameters fall into the intermediate frequency region where neither SPM nor KM are applicable. The IEM co-polarized

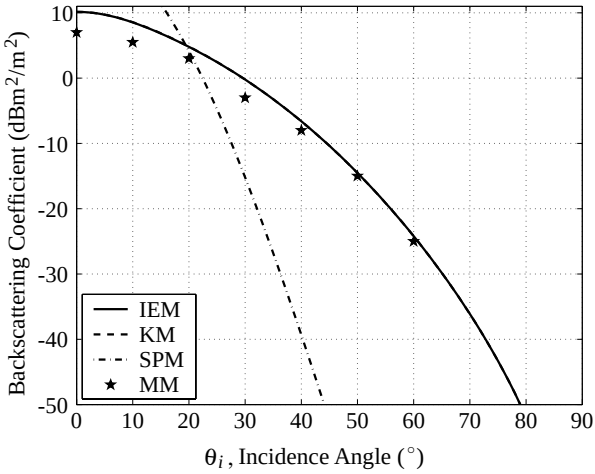

Figure 8. Comparisons of IEM, KM, SPM and MM in the frequency domain where KM is applicable.

backscattering coefficient starts deviating from the SPM solution and approaches the KM one.

In Fig. 8, IEM and SPM values differ significantly because the latter is no longer applicable. However KM is now valid, and its simulation results exactly coincide with those of IEM.

3.1.2. Parametrical Study of the Backscattering Coefficient

The study presented is focused on the evolution of the backscattering coefficient as a function of the surface roughness. An exponential correlated asphalt surface is considered for example at millimeter-wave frequencies (94 GHz). Its RMS height s_z increases regularly whereas correlation length l_c is constant at 2λ. The characteristic parameters of the asphalt surface were collected in [24].

Fig. 9 shows that backscattered power increases with the roughness of the surface, except near the normal incidence where the scattering coefficient decreases when the roughness increases. This may be explained by the fact that the scattering diagram is widening while no extra energy is brought to the system.

Finally, when $s_z = \frac{\lambda}{3}$, no scattering direction is no longer privileged.

A zoom of the behavior of backscattering coefficient near grazing incidence is showed in Fig. 10.

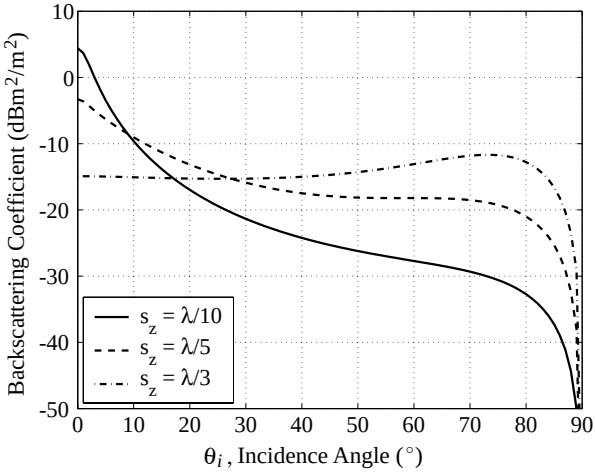

Figure 9. Backscattering by an exponential correlated asphalt surface.

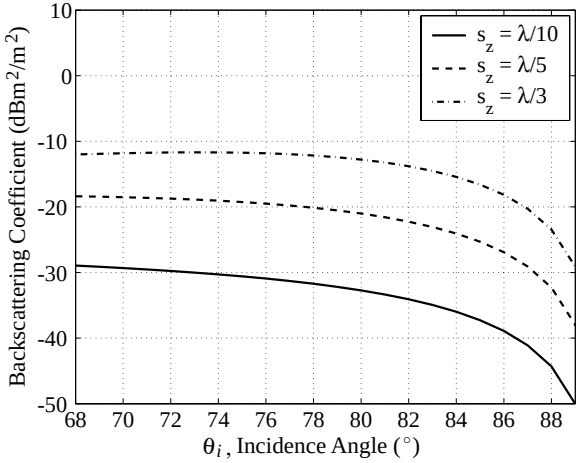

Figure 10. Backscattering near grazing incidence by an exponential correlated asphalt surface.

3.1.3. Comparisons with Experimental Results and Validation

A set of monostatic measurements from known Gaussian correlated, dielectric smooth to rough surfaces were reported by the the European Microwave Signature Laboratory (EMSL), installed at the Joint Research Centre (JRC) in Ispra, Italy [25–27]. The surface considered

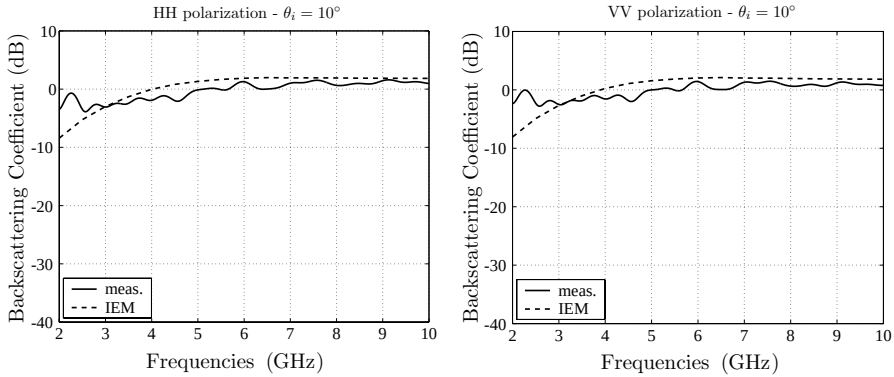

Figure 11. Comparison of IEM with experimental HH and VV measurements at incident angle of 10°.

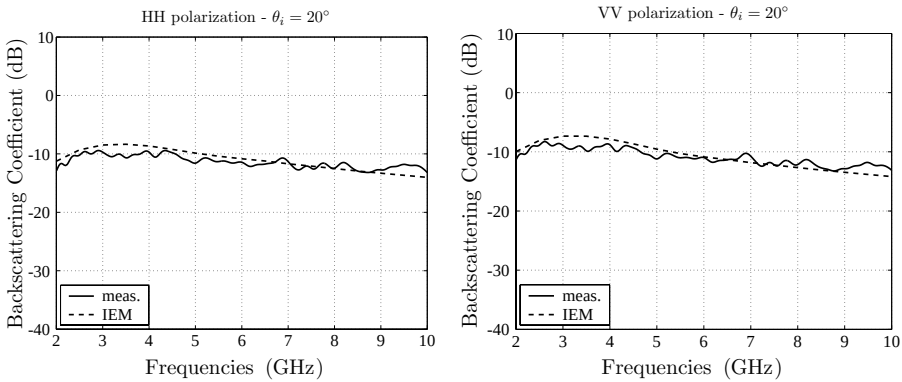

Figure 12. Comparison of IEM with experimental HH and VV measurements at incident angle of 20°.

in these papers presents a RMS height of 4 mm and a correlation length of 60 mm. Polarimetric backscattering measurements proposed were performed between 10° and 30° in co-polarization over a range of frequencies from 2 to 10 GHz.

Figs. 11 to 13 show comparisons between IEM predictions and experimental measurements for HH and VV polarizations. Good agreement is obtained at each angle and for the two polarizations. However, at an incidence of 30°, and above 8 GHz, theoretical results begin to underestimate experimental coefficients; experimental data tend to a constant value whereas the model predicts a decreasing of

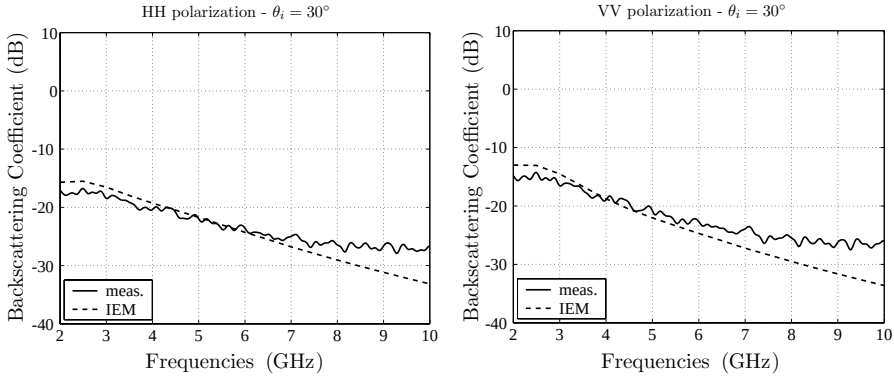

Figure 13. Comparison of IEM with experimental HH and VV measurements at incident angle of 30°.

the backscattering coefficient. For these values, the proximity of the noise floor of the experimental setup can be a possible explanation of these discrepancies.

3.2. The Bistatic Case

3.2.1. Comparisons with SPM and KM

This study is led according to the numerical results obtained by Fung in [1]. As in this article, Fig. 14 shows a good agreement between IEM and SPM predictions in the frequency domain where this latter is applicable, except for large scattering angles ($\theta_s > 60°$).

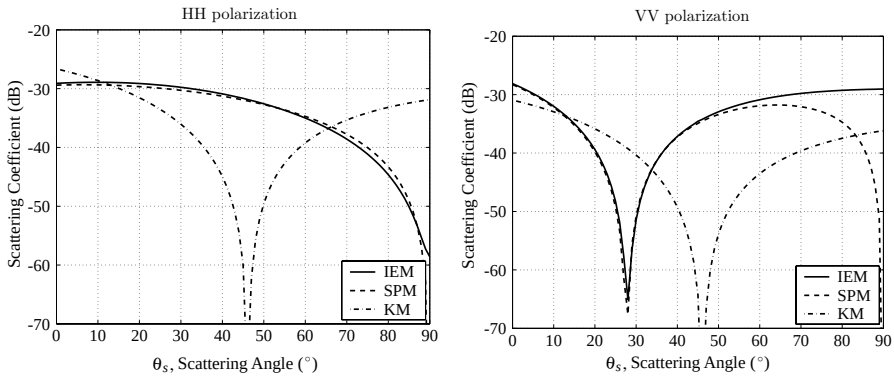

Figure 14. Comparison between IEM, SPM and KM at a frequency of 4.7 GHz.

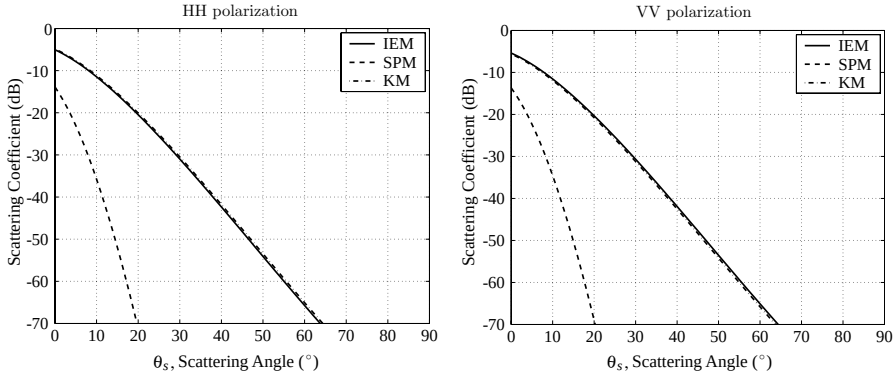

Figure 15. Comparison between IEM, SPM and KM at a frequency of 14.3 GHz.

In Fig. 15, frequency is increased from 4.7 GHz to 14.3 GHz, KM is now valid, and, as it is also noticed in monostatic configuration, IEM and KM predictions exactly coincide in the two polarizations.

3.2.2. Comparisons with an Exact Method

This section concerns the study of the bistatic scattering by a rectangular perfectly conducting smooth surface. IEM results are confronted with those of a software available at the Electromagnetic and Radar Department (DEMR) of ONERA and based on the Method of Moments (MM).

This study is carried out at a frequency of 35 GHz. The illuminated area was delimited at a squared surface $A_0 = 8\lambda \times 8\lambda$ in order to find a good compromise between a reasonable computing time by the MM and large enough dimensions for the use of Physical Optics model.

Fig. 16 shows the results obtained. IEM gives results which are in good agreement with those of the method of reference. The most significant errors appear near grazing observation angles. Indeed, it is at grazing angles that edge effects (not taken into account in the IEM model) become important, so they are less and less negligible. The dimensions of the illuminated surface, which are limited by the exact method, are not large enough compared with the wavelength to allow to neglect edge effects.

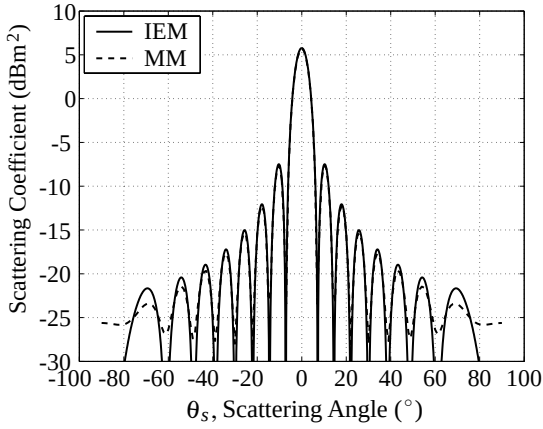

Figure 16. Comparisons of IEM scattering coefficient with MM simulations in the case of a smooth conducting surface.

3.2.3. Parametrical Study of the Scattering Coefficient

To compare the evolution according to the surface roughness, of the coherent (17) and incoherent (50) scattering coefficients, their variations are represented in the upper half-space. The incidence angle is 40°, the scattering angle and the scattering azimuthal angle respectively vary between 0° and 90° and 0° and 360°, to describe the upper half-sphere. The cases of a smooth, then two rough surfaces are illustrated. The frequency is 94 GHz.

In the case of the smooth surface ($s_z = 0\,\text{mm}$), the principal lobe is really noticeable and exactly corresponds to the specular direction (Fig. 17).

When the surface roughness increases ($0\,\text{mm} < s_z < \frac{\lambda}{3} = 1.0\,\text{mm}$), the coherent scattering regularly decreases whereas the incoherent scattering gradually increases, the power being scattered in the other directions (Fig. 18).

Finally, when the surface is very rough ($s_z = \frac{\lambda}{3} = 1.0\,\text{mm}$), the scattering diagram is widened, the incoherent component increases until there is nearly no privileged direction of scattering (Fig. 19).

3.2.4. Comparisons with Experimental Results and Validation

A set of bistatic measurements from known Gaussian correlated, perfectly conducting surfaces were reported by the EMSL in [28]. The surface considered presents the same roughness characteristic as the one concerned in the backscattering study. The measurements are

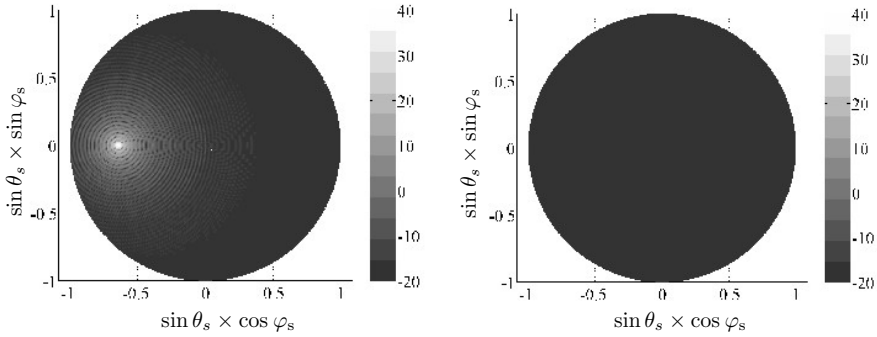

Figure 17. Coherent and incoherent scattering coefficients (in dBm^2) from a smooth surface at 94 GHz - $s_z = 0$ mm.

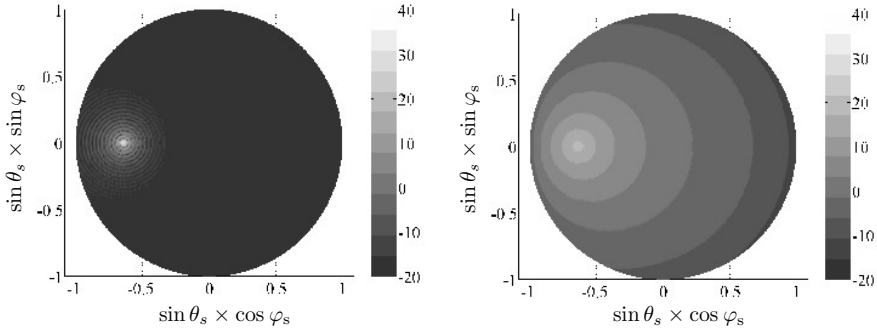

Figure 18. Coherent and incoherent scattering coefficients (in dBm^2) from a moderately rough surface at 94 GHz - $s_z = \frac{\lambda}{10} = 0.3$ mm.

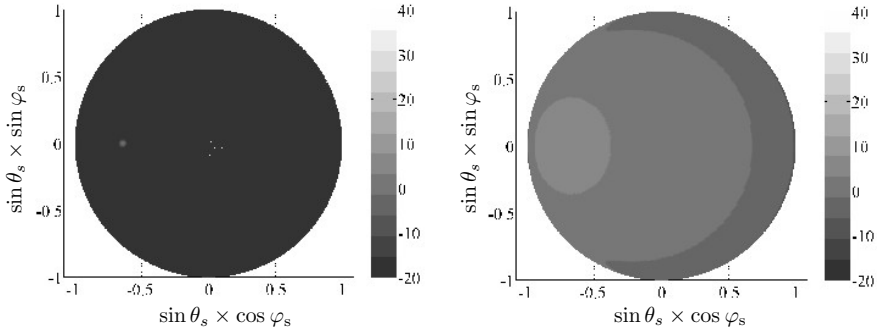

Figure 19. Coherent and incoherent scattering coefficients (in dBm^2) from a rough surface at 94 GHz - $s_z = \frac{\lambda}{3} = 1.0$ mm.

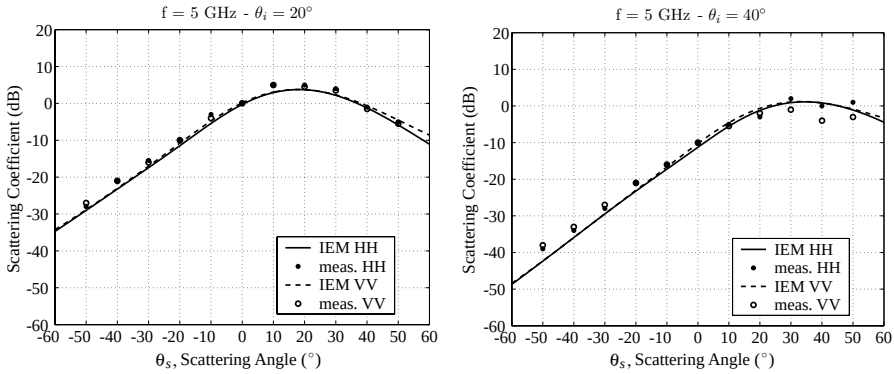

Figure 20. Comparison between IEM and experimental HH and VV measurement at 5 GHz and incidences of 20° and 40°.

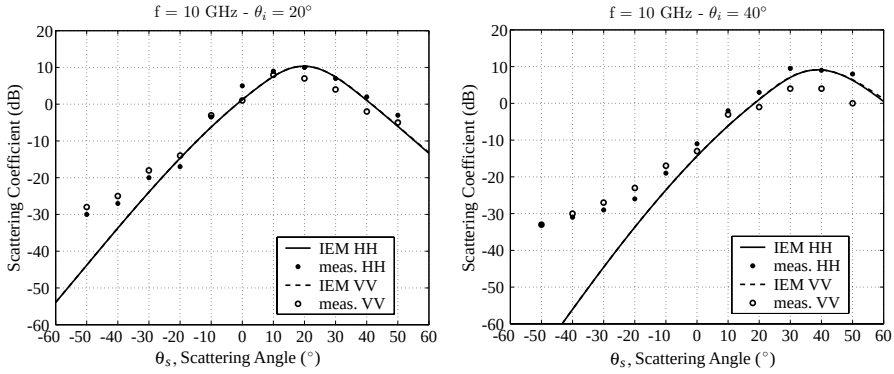

Figure 21. Comparison between IEM and experimental HH and VV measurement at 10 GHz and incidences of 20° and 40°.

taken at different frequencies at incidences of 20° and 40°.

Comparison between IEM predictions and those bistatic measurements is proposed at 5GHz and 10GHz, respectively on Figs. 20 and 21. At the lower frequency, the model well reproduces experimental data for HH and VV polarizations. At the upper frequency, the same trend is observed between the two types of results for HH polarization and scattering angle higher than $-20°$; for $-60° < \theta_s < -20°$, the model underestimates experimental values, especially in VV polarization.

3.3. Conclusion on the Numerical Study

In this section, numerical studies on scattering coefficient were carried out. In monostatic and bistatic configurations, it is proved that IEM tends to SPM and KM in the frequency domains where these latter are applicable. It is verified on the whole frequency band that IEM is in good agreement with a reference method (MM). It is thus confirmed that IEM is applicable over the whole frequency band and presents a wider range of applicability with respect to other classical models such as SPM or KM.

Moreover, a study of the variations of the bistatic scattering coefficient allows to highlight the behavior, according to the degree of roughness, of the coherent and incoherent scattering components.

Finally, both in monostatic and in bistatic configurations, good agreement is obtained between experimental data reported by the the European Microwave Signature Laboratory (EMSL), installed at the Joint Research Centre (JRC) in Ispra, Italy and our simulations results. All these results are an encouraging milestone of validation of the IEM model.

4. EXPERIMENTAL ILLUSTRATIONS OF THE SURFACE SCATTERING COEFFICIENT BEHAVIOR AND IEM VALIDATION

4.1. Presentation of the Measurements Setup

The measurements setup [29], used for the experimentation, is operating in the Ka-band (28–40 GHz), and is presented in Fig. 22. It is composed of two identical ellipsoidal bifocal reflectors whose diameters and focal distances are respectively equal to 30 cm and 37 cm and a sample-holder which allows to characterize samples of $297 \times 297\,\mathrm{mm}^2$ dimensions.

Each ellipsoid is illuminated by a pyramidal horn, placed in its first focus. The beam generated at the second focus is Gaussian with a diameter close to 2λ at -3 dB aperture lobe. The variation of phase in the focal plane is much lower than $45°$.

The antennas are laid out so that their second focus coincide; the sample-holder is placed at this focus. It is located on a revolving pot which allows the rotation of the incidence plane.

The antennas can turn around the radioelectric axis, which allows measurements according to polarization. The network analyser, the rotary translators and positioners are operating through a micro-calculator.

Figure 22. Measurements setup in Ka-band.

The setup allows, for any type of material, to make measurements either in transmission or in reflection, according to the frequency, the polarization, the incidence angle, the observation angle between the two antennas.

4.2. Characterization of the Samples

For this experimental study, the *Laboratoire Régional des Ponts et Chaussées* (LRPC) in Toulouse (France) provided us two types of samples of road surfaces. The two samples, which will thereafter be named ES and BBTM, are representative of 90% of the roadways of the French road network. They were taken on the surface wearing various roads. It is the part which supports the aggressions of surface. The wearing consists of a surface treatment in which one or several layers of aggregates are uniformly widespread on the roadway. The materials of roadways are always composed of granular materials (sands), to which a hydraulic binder (cement) or hydrocarbon (bituminizes) is possibly added. An other characteristic of these materials is their compactness which determines their porosity (it is often about only of a few percent).

As they were cut out with a diamond saw, the samples present a smooth face and a rough face which are separately studied.

Figure 23. Smooth side of ES.

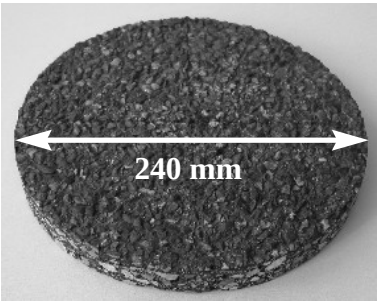

Figure 24. Rough side of ES.

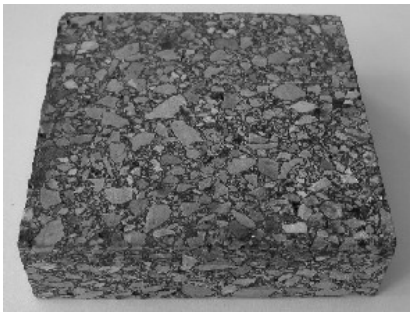

Figure 25. Smooth side of BBTM.

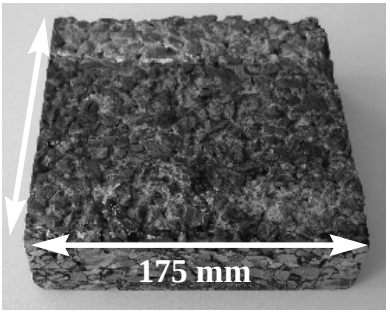

Figure 26. Rough side of BBTM.

4.2.1. Presentation

ES is a cylindrical sample. Its two faces are presented below in Figs. 23 and 24. However let us underline that the smooth ES face presents some irregularities due to its sawing up. The average thickness of the ES sample is about 26.5 mm.

The other sample (BBTM) has undergone rigidity tests, and presents, on its rough face, a rolling band. Measurements in back-scattering and in reflection were made on this band. The photographs in Figs. 25 and 26 present the smooth and rough faces of the BBTM sample. The average thickness in the rolling band is about 47.8 mm.

4.2.2. Roughness and Dielectric Parameters Measurement

The heights of the irregularities on the surface of the samples are measured with a mechanical roughometer. The roughness profile is collected according to a diameter in the case of ES, and according to

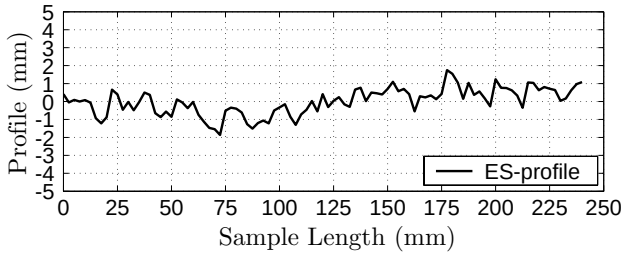

Figure 27. Rough profile of ES.

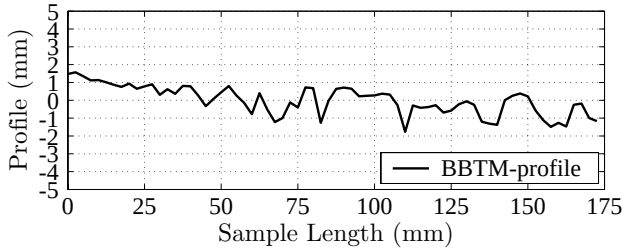

Figure 28. Rough profile of BBTM.

the central line of the rolling band in the case of BBTM.

Figs. 27 to 32 give various information about the roughness of the samples.

First the rough profiles of the samples are plotted in Figs. 27 and 28. The RMS height s_z is deduced from the roughness profile as it corresponds to standard deviation of the heights of the irregularities. In order to determine an average value and the interval of variation in which s_z moves, several measurements were taken at different places on each sample.

The measured height distribution is then confronted in Figs. 29 and 31 with those of a Gaussian process having the same RMS height. Lastly, the evolution of the correlation coefficient C(R) corresponding to the profile is shown on the curves of Figs. 30 and 32. The correlation length can be evaluated as it corresponds to the classical distance for which C(R) is equal to 1/e. The experimental curve were compared with those of exponential and Gaussian correlation coefficients.

Within the framework of the simulation tool validation, the studied surfaces are supposed to present Gaussian height distributions and exponential autocorrelation functions.

Some informations on the dielectric characteristics of the samples are also brought. The dielectric constant is calculated, at each

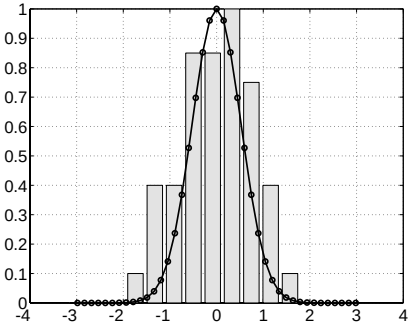

Figure 29. Height distribution on ES rough side.

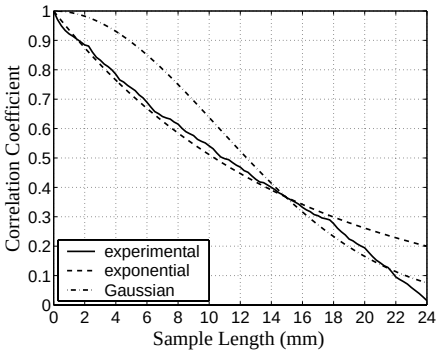

Figure 30. Correlation coefficients of ES.

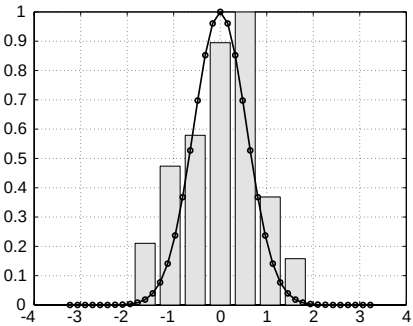

Figure 31. Height distribution on BBTM rough side.

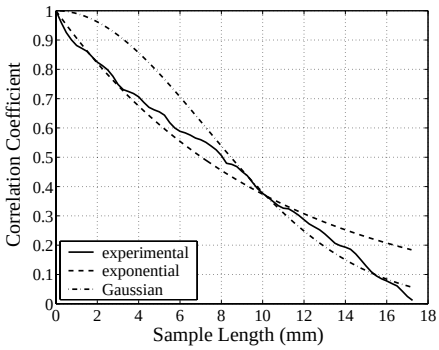

Figure 32. Correlation coefficients of BBTM.

frequency, from measurements in transmission and in reflection and with an adapted software available at the DEMR and based on Physical Optics. Thus, for each sample, an average permittivity is determined on the Ka band.

Finally, the various characteristic parameters of the three studied samples are listed in Table 2.

No variation interval is given for correlation lengths because these parameters have no significant influence on the values of the scattered coefficients in the specular directions where our measurements are performed.

Table 2. Characteristics of the samples.

Samples	ES	BBTM
s_z (mm)	$0.7 \pm 10\%$	$0.8 \pm 10\%$
l_c (mm)	14.5	10.0
ε_r	$4.4 - 0.3i$	$4.8 - 0.5i$
Thickness (mm)	26.5	47.8

4.3. Results of the Experimental Study in Backscattering and Forward Scattering

The results obtained, for each sample, by the studies in backscattering at normal incidence and in forward scattering for an incidence angle of 30° are presented in this section.
Several measurements are made at various places on the two sides of the samples in order to realize the randomness of the scattering by rough surfaces. Let us recall, however, that on the BBTM sample, all the measures are made in the rolling band.

Within the framework of measurements on the smooth faces of the samples, we also compared the experimental values and the results of simulations by IEM with those obtained by Physical Optics, which allows an additional validation of the simulation tools.

The results in HH polarization are proposed on this paper.

4.3.1. Case of ES Sample

• Smooth side of ES

In backscattering as in reflection (Figs. 33 and 34), the theoretical coefficients surestimate the measured scattering coefficients which depend on the frequency. This is explained by the fact that the smooth ES face presents some irregularities caused by its cutting. The addition of a low roughness given by adequate values of s_z and l_c would allow to take them into account and thus to compensate for the gap between the two types of results.

On the other hand, the results obtained by IEM correspond to an average of those of Physical Optics. As a matter of fact, the ES sample has a small thickness and cannot be regarded as semi-infinite on the concerned frequency band. So a fraction of the incident wave penetrates in the medium and is reflected on the second interface. The resulting field is added in a vectorial way to the field reflected

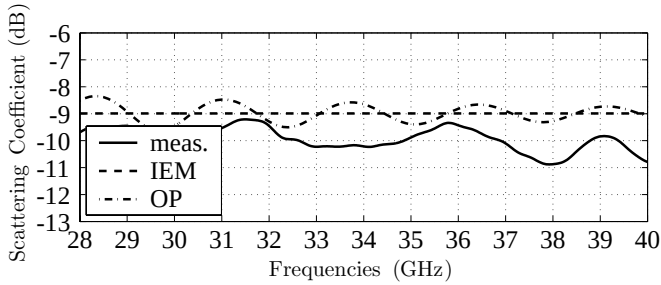

Figure 33. Backscattering from smooth side of ES.

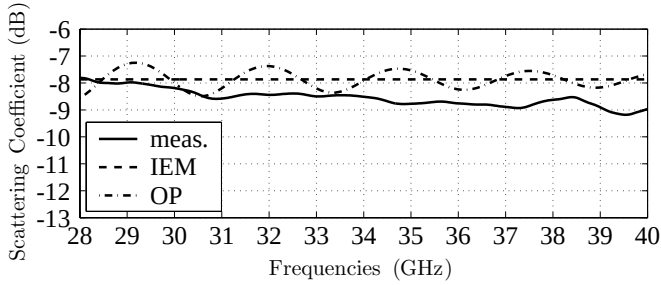

Figure 34. Forward scattering from smooth side of ES.

by the first interface. This leads to the oscillations observed on the experimental curves and those of Physical Optics.

• Rough side of ES

In backscattering and reflection, Figs. 35 and 36 show that the results given by IEM correspond, on the Ka-band, to an average of the experimental results.

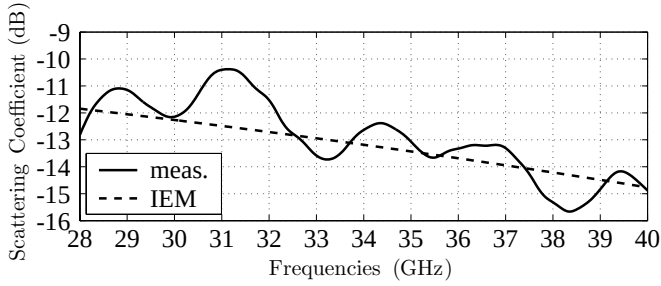

Figure 35. Backscattering from rough side of ES.

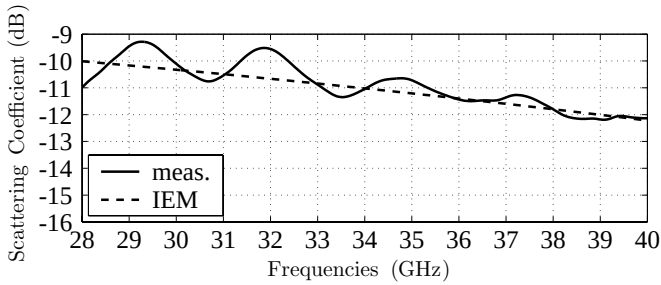

Figure 36. Forward scattering from rough side of ES.

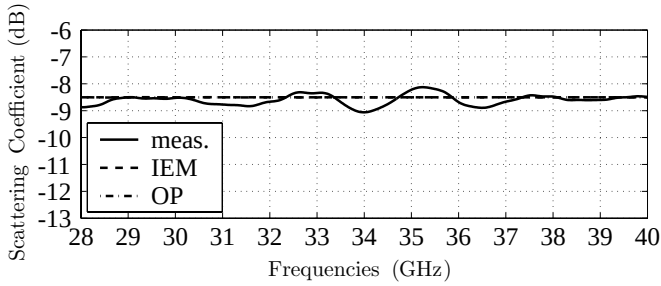

Figure 37. Backscattering from smooth side of BBTM.

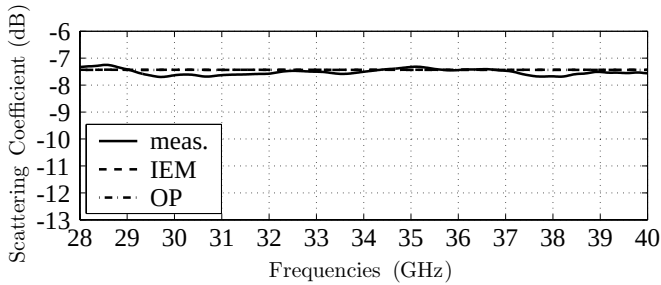

Figure 38. Forward scattering from smooth side of BBTM.

4.3.2. Case of BBTM Sample

• Smooth side of BBTM

In the case of the smooth surface of the BBTM, in backscattering as in forward scattering (Figs. 37 and 38), the simulation results and experimental data are in very good agreement.

On the other hand, Physical Optics and IEM results exactly coincide because no reflection occurs at the second interface of the BBTM sample and the material behaves on the Ka-band as a semi-

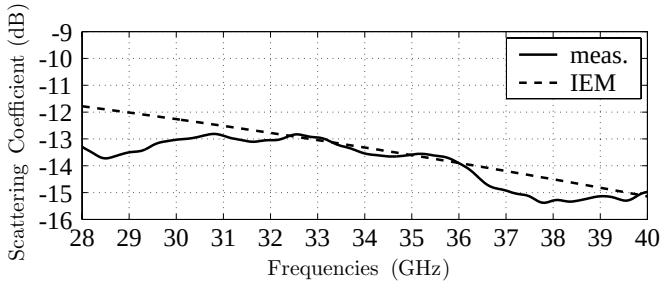

Figure 39. Backscattering from rough side of BBTM.

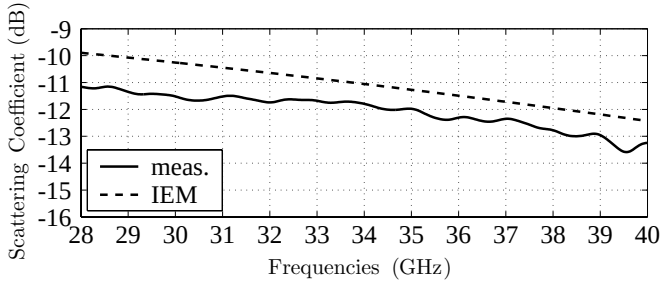

Figure 40. Forward scattering from rough side of BBTM.

infinite medium.

• Rough side of BBTM

In backscattering (Fig. 39), the results given by IEM are comparable with the experimental measurements. In forward scattering (Fig. 40), experimental data are overestimated by the model. A possible explanation is the fact that the illuminated surface appears a little larger because of incidence; moreover the non-uniformity of roughness on extended surface is constated.

4.3.3. Conclusion on This Experimental Study and IEM Validation

The discrepancies sometimes observed are due to various types of factors:

- The maximum errors of accuracy inherent in the system of measurement in the case of a perfect sample are summarized in Table 3. Currently, the accuracy of measurements depends on the state of the surface, the parallelism of the sample faces and the errors caused due to the instrumentation.

Table 3. Defects of instrumentation.

Illumination Level (dB)	Accuracy for incidence between 0° and 30°
0 to -1	±0.02
-1 to -3	±0.1
-3 to -10	±0.2
-10 to -40	±0.5
beyond -40	$> \pm 1$

- Because of the tests undergone elsewhere and of their sawing, the faces of the samples present lacks of flatness. These defects can involve some errors in measurements, as the plane of measurement on the sample does not exactly correspond to the reference plane fixed during the calibration of the system.
- Lastly, the quasi-totality of the noticed differences are due to the difficulties encountered during the characterization of the samples. The measured dielectric and roughness paremeters do not exactly describe the road samples, which are very difficult to characterize because of the complexity of their manufacturing.

However, despite these difficulties, good agreements are generally obtained between experimental measurements and the simulated results by IEM.

5. CONCLUSION

This paper is devoted to the numerical and experimental validations of the improved version of the Integral Equation Method recently published by Fung, Liu, Chen and Tsay in [1].

First, as an introduction, the chronology of the successive improvements made to the IEM theoretical formulation is briefly detailed. Then, the major steps of the surface scattering coefficient calculation by IEM are enumerated in the following section.

In the third part, numerical validations of the model have been investigated. The IEM simulation results are compared with those of Method of Moments (MM) on a wide frequency range, and with Small Perturbation Method (SPM) and Kirchhoff Model (KM), in the frequency domain where these latter are applicable. It is, thus, verified and confirmed that IEM is applicable over the whole frequency band and tends to bridge the gap between SPM and KM.

Moreover, parametrical study of the surface scattering coefficient is carried out in monostatic and bistatic cases. So, it is assessed that the backscattered power increases with the surface roughness until no scattering direction is no longer privileged. On the other hand, the study of the variations of the bistatic scattering coefficient allows to highlight the behavior, according to the roughness degree, of the coherent and incoherent scattering components.

Finally, both in monostatic and in bistatic configurations, good agreement is obtained between experimental data reported by the European Microwave Signature Laboratory (EMSL), installed at the Joint Research Center (JRC) in Ispra, Italy and IEM simulations results. IEM validation is achieved by confronting the model predictions with experimental data collected during measurements on road surfaces at the Electromagnetism and Radar Department (DEMR) of ONERA-Toulouse (France). Either in backscattering as in forward scattering, the overall agreement between the model and data is very satisfying.

These numerical and experimental validations allow to conclude that the IEM model suit predict the scattering from random smooth to moderate rough surfaces, on a wide range of frequencies and angular observations.

ACKNOWLEDGMENT

We would like to express deep gratitude to Mrs. Maryse Lopez of DEMR and to Mr. Lafon and M. Lissraud of the "Laboratoire Régional des Ponts et Chaussées" for the time they give us for the experimental validation of IEM and for their helpful comments.

We are also most indebted to Mr. Joaquim Fortuny of the JRC for the help he provided us to access EMSL data base.

APPENDIX A. THE FIELD COEFFICIENTS EXPRESSIONS

In this section, the expressions of the Kirchhoff and complementary field is given in the general case. It is advised to refer to page 167 in [9], as the same set of coordinates and unit vectors are used as reference.

A.1. Expressions of Kirchhoff Coefficients

The Kirchhoff coefficients expressions f_{qp}, which allow to calculate the Kirchhoff scattering coefficient, are given below, for each co and cross

polarizations by (A1), (A2), (A3) and (A4).

$$f_{\mathrm{hh}} = -\frac{\mathcal{R}_{\mathrm{h}}}{\cos\theta_{\mathrm{s}} + \cos\theta_{\mathrm{i}}}[\sin\theta_{\mathrm{s}}\sin\theta_{\mathrm{i}} - (1+\cos\theta_{\mathrm{s}}\cos\theta_{\mathrm{i}})\cos(\varphi_{\mathrm{s}}-\varphi_{\mathrm{i}})] \quad \text{(A1)}$$

$$f_{\mathrm{vv}} = \frac{\mathcal{R}_{\mathrm{v}}}{\cos\theta_{\mathrm{s}} + \cos\theta_{\mathrm{i}}}[\sin\theta_{\mathrm{s}}\sin\theta_{\mathrm{i}} - (1+\cos\theta_{\mathrm{s}}\cos\theta_{\mathrm{i}})\cos(\varphi_{\mathrm{s}}-\varphi_{\mathrm{i}})] \quad \text{(A2)}$$

$$f_{\mathrm{vh}} = -2\mathcal{R}[\sin(\varphi_{\mathrm{s}} - \varphi_{\mathrm{i}})] \quad \text{(A3)}$$

$$f_{\mathrm{hv}} = 2\mathcal{R}[\sin(\varphi_{\mathrm{s}} - \varphi_{\mathrm{i}})] \quad \text{(A4)}$$

where $\mathcal{R}_{\mathrm{h}}$ and $\mathcal{R}_{\mathrm{v}}$ are horizontal and vertical reflection coefficients and $\mathcal{R} = \frac{\mathcal{R}_{\mathrm{v}} - \mathcal{R}_{\mathrm{h}}}{2}$.

A.2. Expressions of Complementary Coefficients

The co and cross polarized complementary coefficient expressions are calculated on Appendix 4B in [9]. The general expressions of the C_{i} and B_{i} coefficients (A5 to A16) are given below when the phase term is removed in the Green function (1).

• C_{i} coefficients

$$\begin{aligned} C_1(\vec{k}_{\mathrm{s}}, \vec{k}_{\mathrm{i}}, rq) &= k\cos(\varphi_{\mathrm{s}} - \varphi_{\mathrm{i}}) \\ &\quad - \frac{k}{(k_{sz}-rq)(k_z+rq)} \times [(k_{sx}+u)\ \cos\varphi_{\mathrm{s}} + (k_{sy}+v)\ \sin\varphi_{\mathrm{s}}] \\ &\quad \times [(k_x+u)\ \cos\varphi_{\mathrm{i}} + (k_y+v)\ \sin\varphi_{\mathrm{i}}] \end{aligned} \quad \text{(A5)}$$

$$\begin{aligned} C_2(\vec{k}_{\mathrm{s}}, \vec{k}_{\mathrm{i}}, rq) &= \cos\theta_{\mathrm{i}}\ \cos(\varphi_{\mathrm{s}} - \varphi_{\mathrm{i}})\ rq \\ &\quad + \frac{\cos\theta_{\mathrm{i}}}{k_z+rq}[(k_x+u)\sin\varphi_{\mathrm{i}} - (k_y+v)\cos\varphi_{\mathrm{i}}][\sin\varphi_{\mathrm{s}}u - \cos\varphi_{\mathrm{s}}v] \\ &\quad + \frac{\sin\theta_{\mathrm{i}}}{k_z+rq}\ [(k_x+u)\ \cos\varphi_{\mathrm{s}} + (k_y+v)\ \sin\varphi_{\mathrm{s}}]\ rq \\ &\quad - \frac{\cos\theta_{\mathrm{i}}}{k_{sz}-rq}[(k_{sx}+u)\cos\varphi_{\mathrm{s}} + (k_{sy}+v)\sin\varphi_{\mathrm{s}}][\cos\varphi_{\mathrm{i}}u + \sin\varphi_{\mathrm{i}}v] \\ &\quad - \frac{\sin\theta_{\mathrm{i}}}{(k_{sz}-rq)(k_z+rq)}[(k_{sx}+u)\cos\varphi_{\mathrm{s}} + (k_{sy}+v)\sin\varphi_{\mathrm{s}}] \\ &\quad \times [(k_x+u)u + (k_y+v)v] \end{aligned} \quad \text{(A6)}$$

$$\begin{aligned} C_3(\vec{k}_{\mathrm{s}}, \vec{k}_{\mathrm{i}}, rq) &= \left\{ \frac{\cos\theta_{\mathrm{i}}}{k_z+rq}[(k_x+u)\ \cos\varphi_{\mathrm{i}} + (k_y+v)\ \sin\varphi_{\mathrm{i}}] - \sin\theta_{\mathrm{i}} \right\} \\ &\quad \times \left\{ \frac{1}{k_{sz}-rq}[(k_{sx}+u)\ \cos\varphi_{\mathrm{s}} + (k_{sy}+v)\ \sin\varphi_{\mathrm{s}}]\ rq \right. \end{aligned}$$

$$+\left[\cos\varphi_{\rm s}\,u+\sin\varphi_{\rm s}\,v\right]\Bigg\} \tag{A7}$$

$$\begin{aligned}
C_4(\vec{k}_{\rm s},\vec{k}_{\rm i},rq) &= k\ \cos\theta_{\rm s}\ \cos\theta_{\rm i}\ \cos(\varphi_{\rm s}-\varphi_{\rm i})\\
&+\frac{k\ \cos\theta_{\rm s}\ \sin\theta_{\rm i}}{k_z+rq}\ [(k_x+u)\ \cos\varphi_{\rm s}+(k_y+v)\ \sin\varphi_{\rm s}]\\
&+\frac{k\ \sin\theta_{\rm s}\ \cos\theta_{\rm i}}{k_{sz}-rq}\ [(k_{sx}+u)\ \cos\varphi_{\rm i}+(k_{sy}+v)\ \sin\varphi_{\rm i}]\ rq\\
&-\frac{k\cos\theta_{\rm s}\cos\theta_{\rm i}}{(k_{sz}-rq)(k_z+rq)}[(k_{sx}+u)\sin\varphi_{\rm s}-(k_{sy}+v)\cos\varphi_{\rm s}]\\
&\times[(k_x+u)\sin\varphi_{\rm i}-(k_y+v)\cos\varphi_{\rm i}]\\
&+\frac{k\sin\theta_{\rm s}\sin\theta_{\rm i}}{(k_{sz}-rq)(k_z+rq)}[(k_{sx}+u)(k_x+u)+(k_{sy}+v)(k_y+v)]
\end{aligned} \tag{A8}$$

$$\begin{aligned}
C_5(\vec{k}_{\rm s},\vec{k}_{\rm i},rq) &= -\cos\theta_{\rm s}\ \cos(\varphi_{\rm s}-\varphi_{\rm i})\ rq\\
&-\frac{\cos\theta_{\rm s}}{k_z+rq}[(k_x+u)\cos\varphi_{\rm i}+(k_y+v)\sin\varphi_{\rm i}][\cos\varphi_{\rm s}u+\sin\varphi_{\rm s}v]\\
&+\frac{\cos\theta_{\rm s}}{k_{sz}-rq}[(k_{sx}+u)\sin\varphi_{\rm s}-(k_{sy}+v)\cos\varphi_{\rm s}][\sin\varphi_{\rm i}u-\cos\varphi_{\rm i}v]\\
&-\frac{\sin\theta_{\rm s}}{k_{sz}-rq}\ [(k_{sx}+u)\ \cos\varphi_{\rm i}+(k_{sy}+v)\ \sin\varphi_{\rm i}]\ rq\\
&-\frac{\sin\theta_{\rm s}}{(k_{sz}-rq)(k_z+rq)}\ [(k_x+u)\ \cos\varphi_{\rm i}+(k_y+v)\ \sin\varphi_{\rm i}]\\
&\times[(k_{sx}+u)\ u+(k_{sy}+v)\ v]
\end{aligned} \tag{A9}$$

$$\begin{aligned}
C_6(\vec{k}_{\rm s},\vec{k}_{\rm i},rq) &= \frac{1}{(k_z+rq)}\ [(k_x+u)\ \sin\varphi_{\rm i}+(k_y+v)\ \cos\varphi_{\rm i}]\\
&\times\Bigg\{\frac{-\cos\theta_{\rm s}}{(k_{sz}-rq)}\ [(k_{sx}+u)\ \sin\varphi_{\rm s}-(k_{sy}+v)\ \cos\varphi_{\rm s}]\ rq\\
&-\cos\theta_{\rm s}\ [\sin\varphi_{\rm s}\,u-\cos\varphi_{\rm s}\,v]+\frac{\sin\theta_{\rm s}}{(k_{sz}-rq)}\\
&\times[(k_{sx}+u)\ v-(k_{sy}+v)\ u]\Bigg\}
\end{aligned} \tag{A10}$$

• $B_{\rm i}$ coefficients

$$B_1(\vec{k}_{\rm s},\vec{k}_{\rm i},rq) = k\ \cos\theta_{\rm s}\ \sin(\varphi_{\rm s}-\varphi_{\rm i})$$

$$
\begin{aligned}
&- \frac{k\ \sin\theta_{\mathrm{s}}}{(k_{sz}-rq)}\ [(k_{sx}+u)\ \sin\varphi_{\mathrm{i}} - (k_{sy}+v)\ \cos\varphi_{\mathrm{i}}] \\
&- \frac{k\ \cos\theta_{\mathrm{s}}}{(k_{sz}-rq)(k_z+rq)}\ [(k_{sx}+u)\ \sin\varphi_{\mathrm{s}} - (k_{sy}+v)\ \cos\varphi_{\mathrm{s}}] \\
&\times [(k_x+u)\ \cos\varphi_{\mathrm{i}} + (k_y+v)\ \sin\varphi_{\mathrm{i}}] \qquad \text{(A11)}
\end{aligned}
$$

$$
\begin{aligned}
B_2(\vec{k}_{\mathrm{s}},\vec{k}_{\mathrm{i}},rq) = {} & \cos\theta_{\mathrm{s}}\ \cos\theta_{\mathrm{i}}\ \sin(\varphi_{\mathrm{s}}-\varphi_{\mathrm{i}}) \\
& - \frac{\cos\theta_{\mathrm{s}}\ \cos\theta_{\mathrm{i}}}{k_z+rq}\ [(k_x+u)\ \sin\varphi_{\mathrm{i}} - (k_y+v)\ \cos\varphi_{\mathrm{i}}] \\
& \times [\cos\varphi_{\mathrm{s}}\ u + \sin\varphi_{\mathrm{s}}\ v] \\
& + \frac{\cos\theta_{\mathrm{s}}\ \sin\theta_{\mathrm{i}}}{k_z+rq}\ [(k_x+u)\ \sin\varphi_{\mathrm{s}} - (k_y+v)\ \cos\varphi_{\mathrm{s}}]\ rq \\
& - \frac{\cos\theta_{\mathrm{s}}\ \cos\theta_{\mathrm{i}}}{k_{sz}-rq}\ [(k_{sx}+u)\ \sin\varphi_{\mathrm{s}} + (k_{sy}+v)\ \cos\varphi_{\mathrm{s}}] \\
& \times [\cos\varphi_{\mathrm{i}}\ u + \sin\varphi_{\mathrm{i}}\ v] \\
& - \frac{\sin\theta_{\mathrm{s}}\ \cos\theta_{\mathrm{i}}}{k_{sz}-rq}\ [(k_{sx}+u)\ \sin\varphi_{\mathrm{i}} - (k_{sy}+v)\ \cos\varphi_{\mathrm{i}}]\ rq \\
& - \frac{\cos\theta_{\mathrm{s}}\ \sin\theta_{\mathrm{i}}}{(k_{sz}-rq)(k_z+rq)} \\
& \times [(k_{sx}+u)\sin\varphi_{\mathrm{s}} - (k_{sy}+v)\cos\varphi_{\mathrm{s}}][(k_x+u)u + (k_y+v)v] \\
& - \frac{\sin\theta_{\mathrm{s}}\cos\theta_{\mathrm{i}}}{(k_{sz}-rq)(k_z+rq)} \\
& \times [(k_x+u)\sin\varphi_{\mathrm{i}} - (k_y+v)\cos\varphi_{\mathrm{i}}][(k_{sx}+u)u + (k_{sy}+v)v] \\
& - \frac{\sin\theta_{\mathrm{s}}\sin\theta_{\mathrm{i}}}{(k_{sz}-rq)(k_z+rq)}[(k_{sx}+u)(k_y+v) - (k_{sy}+v)(k_x+u)]
\end{aligned}
\qquad \text{(A12)}
$$

$$
\begin{aligned}
B_3(\vec{k}_{\mathrm{s}},\vec{k}_{\mathrm{i}},rq) = {} & \left\{ - \frac{\cos\theta_{\mathrm{i}}}{k_z+rq}[(k_x+u)\cos\varphi_{\mathrm{i}} + (k_y+v)\ \sin\varphi_{\mathrm{i}}] + \sin\theta_{\mathrm{i}} \right\} \\
& \times \left\{ \frac{\cos\theta_{\mathrm{s}}}{k_{sz}-rq}\ [(k_{sx}+u)\ \sin\varphi_{\mathrm{s}} - (k_{sy}+v)\ \cos\varphi_{\mathrm{s}}]\ rq \right. \\
& - \cos\theta_{\mathrm{s}}\ [\sin\varphi_{\mathrm{s}}\ u - \cos\varphi_{\mathrm{s}}\ v] + \frac{\sin\theta_{\mathrm{s}}}{k_{sz}-rq} \\
& \left. \times [(k_{sx}+u)\ v - (k_{sy}+v)\ u] \right\}
\end{aligned}
\qquad \text{(A13)}
$$

$$
B_4(\vec{k}_{\mathrm{s}},\vec{k}_{\mathrm{i}},rq) = -k\ \cos\theta_{\mathrm{i}}\ \sin(\varphi_{\mathrm{s}}-\varphi_{\mathrm{i}})
$$

$$\frac{k\ \sin\theta_{\rm i}}{k_z+rq}\ [(k_x+u)\ \sin\varphi_{\rm i}-(k_y+v)\ \cos\varphi_{\rm i}]$$
$$-\frac{k\ cos\theta_{\rm i}}{(k_{sz}-rq)(k_z+rq)}[(k_{sx}+u)\cos\varphi_{\rm s}+(k_{sy}+v)\sin\varphi_{\rm s}]$$
$$\times[(k_x+u)\ \sin\varphi_{\rm i}-(k_y+v)\ \cos\varphi_{\rm i}] \tag{A14}$$

$$B_5(\vec{k}_{\rm s},\vec{k}_{\rm i},rq)=\sin(\varphi_{\rm s}-\varphi_{\rm i})\,rq$$
$$+\frac{1}{k_z+rq}[(k_x+u)\cos\varphi_{\rm i}+(k_y+v)\sin\varphi_{\rm i}][\sin\varphi_{\rm s}u-\cos\varphi_{\rm s}v]$$
$$+\frac{1}{k_{sz}-rq}[(k_{sx}+u)\cos\varphi_{\rm s}+(k_{sy}+v)\sin\varphi_{\rm s}][\sin\varphi_{\rm i}u-\cos\varphi_{\rm i}v] \tag{A15}$$

$$B_6(\vec{k}_{\rm s},\vec{k}_{\rm i},rq)=\frac{1}{k_z+rq}\ [(k_x+u)\ \cos\varphi_{\rm i}+(k_y+v)\ \sin\varphi_{\rm i}]$$
$$\times\left\{-\frac{1}{k_{sz}-rq}\ [(k_{sx}+u)\ \cos\varphi_{\rm s}+(k_{sy}+v)\ \sin\varphi_{\rm s}]\,rq\right.$$
$$\left.-[\cos\varphi_{\rm s}\,u+\sin\varphi_{\rm s}\,v]\right\} \tag{A16}$$

REFERENCES

1. Fung, A. K., W. Y. Liu, K. S. Chen, and M. K. Tsay, "An improved model for bistatic scattering from rough surfaces," *Journal of Electromagnetic Waves and Applications*, Vol. 16, No. 5, 689–702, 2002.
2. Rice, S. O., "Reflection of electromagnetic waves from slightly rough surfaces," *Communauty of Pure Applied Mathematics*, Vol. 4, 361–378, 1951.
3. Ulaby, F. T., R. K. Moore, and A. K. Fung, *Microwave Remote Sensing Active and Passive – II*, Artech House, 1982.
4. Ogilvy, J. A., *Theory of Wave Scattering from Random Rough Surfaces*, Adam Hilger, 1991.
5. Voronovich, A. G., "Small-slope approximation in wave scattering by rough surfaces," *Soviet Physics JETP*, Vol. 62, 65–70, 1985.
6. Voronovich, A. G., *Wave Scattering from Rough Surfaces*, 2nd ed., Springer-Verlag, 1999.
7. Warnick, K. F. and W. C. Chew, "Numerical simulations methods for rough surface scattering — Topical Review," *Waves in Random Media*, Vol. 11, R1–R30, 2001.

8. Fung, A. K., Z. Li, and K. S. Chen, "Backscattering from a randomly rough dielectric surface," *IEEE Transactions on Geoscience and Remote Sensing*, Vol. 30, No. 2, 356–369, March 1992.
9. Fung, A. K., *Microwave Scattering and Emission Models and Their Applications*, Artech House, 1994.
10. Poggio, A. J. and E. K. Miller, "Integral equation solutions of three dimensional scattering problems," *Computer Techniques for Electromagnetics*, Pergamon, Chapter 4, 159–264, 1963.
11. Hsieh, C.-Y., A. K. Fung, G. Nesti, A. J. Sieber, and P. Coppo, "A further study of the IEM surface scattering model," *IEEE Transactions on Geoscience and Remote Sensing*, Vol. 35, No. 4, 901–909, July 1997.
12. Hsieh, C.-Y. and A. K. Fung, "Application of an extented IEM to multiple surface scattering and backscatter enhancement," *Proc. IGARSS '97'*, Vol. 2, 702–704, July 1997.
13. Hsieh, C.-Y. and A. K. Fung, "Application of an extented IEM to multiple surface scattering and backscatter enhancement," *Journal of Electromagnetic Waves and Applications*, Vol. 13, 121–135, 1999.
14. Chen, K. S., T. D. Wu, M. K. Tsay, and A. K. Fung, "A note on the multiple scattering in an IEM model," *IEEE Transactions on Geoscience and Remote Sensing*, Vol. 38, No. 1, 249–256, January 2000.
15. Alvarez-Perez, J. L., "An extension of the IEM/IEMM surface scattering model," *Waves in Random Media*, Vol. 11, 307–329, March 2001.
16. Combes, P. F., *Micro-Ondes Tome 2: Circuits Passifs, Propagation, Antennes*, Dunod, 1997.
17. Li, Z. and A. K. Fung, "A reformulation of surface field integral equation," *Journal of Electromagnetic Waves and Applications*, Vol. 5, No. 2, 195–203, 1991.
18. Chen, M. F. and A. K. Fung, "A numerical study of the regions of validity of the Kirchhoff and small-perturbation rough surface scattering models," *Radio Science*, Vol. 23, No. 2, March 1988.
19. Khenchaf, A., "Modélisation électromagnétique, radar bistatique et traitement de l'information — Habilitation à diriger des recherches," Université de Nantes, December 2000.
20. Koudogbo, F., "Etude des diffusions de surface et de volume par une surface rugueuse dielectrique. Calcul des interactions entre un objet 3D et une surface naturelle," Université Paul Sabatier,

November 2002.

21. Hsieh, C.-Y., "Multiple scattering from randomly rough surfaces," University of Texas at Arlington, April 1996.
22. Hsieh, C.-Y., "Dependence of backscattering enhancement from randomly very rough surfaces," *Proc. IGARSS '99'*, Vol. 4, 2197–2199, June 28–July 2, 1999.
23. Hsieh, C.-Y., "Angular dependence of backscattering enhancement from randomly very rough surfaces," *Chinese Journal of Physics*, Vol. 38, No. 3-I, 491–515, June 2000.
24. Li, E. S. and K. Sarabandi, "Low grazing incidence millimeter-wave scattering models and measurements for various road surfaces," *IEEE Transactions on Antennas and Propagation*, Vol. 47, No. 5, 851–861, May 1999.
25. Coppo, P., D. Tarchi, and M. Weinberger, "An experimental model for surface scattering models validation at the European Microwave Signature Laboratory," *Proc. IGARSS '95'*, Vol. 2, 930–932, July 1995.
26. Nesti, G., P. Coppo, M. Hallikainen, M. Mancini, P. Troch, and M. von Shönermark, "Experimental research at the EMSL on scattering properties of non vegetated terrains," *Proc. IGARSS '95'*, Vol. 3, 2020–2022, July 1995.
27. Nesti, G., J. Fortuny, and J. M. Lopez-Sanchez, "Polarimetric microwave remote sensing experiments at the EMSL," *IEEE Geoscience and Remote Sensing Society Newsletter*, 6–11, March 2000.
28. Marcelloni, M., G. Nesti, P. Pampaloni, S. Sigismondi, D. Tarchi, and S. Lolli, "Experimental validation of surface scattering and emission models," *IEEE Transactions on Geoscience and Remote Sensing*, Vol. 38, No. 1, 459–469, January 2000.
29. Bolioli, S. and M. Lopez, "Microwave material characterization using focused systems," *Proc. PIERS*, Nantes, France, 1998.

Fifamè Koudogbo received the *Diplôme d'Etudes Approfondies* (Postgraduate degree) in Microwave and Optical Telecommunications and the Ph.D. degree in Microwave Electronics, both from the Paul Sabatier University (UPS) of Toulouse (France), respectively in 1998 and in 2002. During her thesis, she worked at the Electromagnetic and Radar Department of the *Office National d'Etudes et de Recherches Aérospatiales* (ONERA), her studies were there dedicated to the diffraction of electromagnetic waves by natural and manmade dielectric or metallic rough surfaces. She also investigated the study of the

coupling between a target and a rough surface. She is now working as post-doctoral researcher at the Avionics and Systems Department (DAS) of the *Ecole Nationale Supérieure d'Ingénieurs de Constructions Aéronautiques* (ENSICA), in Toulouse (France) where her current work is focused on modeling the cross-polarized scattering coefficient from slighlty to very rough surfaces, and applying the results obtained to the calculation of a wave depolarization by a military vehicle.

Paul-François Combes received the *Doctorat de* 3^{ieme} *cycle* and the *Doctorat d'Etat es Sciences* from the Toulouse University, respectively in 1968 and 1978. Since 1980, he had been a Professor of microwave and Head of the Microwave Antennas and Devices Laboratory of the Paul Sabatier University of Toulouse. He is also in charge of the doctoral training in "Microwave and Optical Telecommunications". He has been the Supervisor of 30 doctoral theses of the Paul Sabatier University in Toulouse and is actually conducting three theses. He is author and/or co-author of about 100 publications covering the fields of reflector and arrays antennas, propagation of electromagnetic waves, radar, radiometric and polarimetric devices for millimeter waves. In addition, he is the author of 8 books, including *Microwave Transmission for the telecommunications* (New York: Wiley, 1991 2nd ed., 1995) and *Micro-ondes: Lignes, Guides et Cavités–Volume 1* and *Micro-ondes: Circuits Passifs, Propagation, Antennes–Volume 2* (Paris, France: Dunod, 1996, 1997, in French).

Henri-José Mametsa received the Diploma in Telecommunication Engineering and the Ph.D. degree in Electronics from the *Ecole Nationale des Télécommunications de Bretagne* (France) in 1984 and 1986 respectively. During two years he worked as engineer in the Antennas Design Department of Thomson-CGR. In 1987, he joined the Electromagnetic and Radar Department of the *Office National d'Etudes et de Recherches Aérospatiales* (ONERA) where he has been working in different studies on electromagnetic scattering problems. In 1995, he spent a year on sabbatical at the Defence Research Establishment in Ottawa (Canada) where he worked on remote sensing polarimetry. His current research interests include modelling electromagnetic scattering from man made targets and natural media. Principal applications were developed in the asymptotic electromagnetic formulations coupling with the shooting and bouncing rays technique. He co-directed 6 Ph.D. students during the last 12 years.